APPLICATION OF THE FINITE DIFFERENCE METHOD IN THE STUDY OF WAVE PROPAGATION IN A BOREHOLE

by

Federico Pardo Casas

Licenciado en Física (1979)
Bachiller en Física (1977)
Universidad Nacional de Ingeniería
Lima, Perú

SUBMITTED TO THE DEPARTMENT OF EARTH, ATMOSPHERIC, AND PLANETARY SCIENCES IN PARTIAL FULFILLMENT OF THE REQUIREMENTS FOR THE DEGREE OF

MASTER OF SCIENCE

in

Earth and Planetary Science

at the

MASSACHUSETTS INSTITUTE OF TECHNOLOGY

August, 1984

Signature of Author .....
Department of Earth, Atmospheric, and Planetary Sciences
August 10, 1984

Certified by .....
M. Nafi Toksoz
Thesis Advisor

Accepted by .....
Theodore R. Madden
Chairman
Departmental Committee on Graduate Students

APPLICATION OF THE FINITE DIFFERENCE METHOD IN THE STUDY OF WAVE PROPAGATION IN A BOREHOLE

by

FEDERICO PARDO CASAS

Submitted to the department of Earth, Atmospheric and Planetary Sciences on August, 1984 in partial fulfillment of the requirements for the degree of Master of Science in Geophysics

ABSTRACT

Synthetic seismograms of elastic wave propagation in a fluid-filled borehole were generated using the finite difference method to later understand the effect of variations in the geometry or properties of the borehole. A detailed comparison between the seismograms generated by the finite difference technique and the discrete wavenumber summation technique showed that the body waves (refracted P and S waves) are identical, while the guided waves showed a slight difference in both phase and amplitude. These differences are believed to be due to the dispersion generated by the finite difference method. We have studied the depth of investigation of the refracted body waves in an invaded or damaged borehole using the conventional ray theory approach and compared it to the finite difference methods. The results show that the minimum source-receiver separation necessary to observe the unaltered formation depends on both the velocity gradient and the lowest and highest velocity of the damaged zone. Models calculated for invaded or flushed zones show the effects of invasion on full waveforms. Generally the effect on velocities is small. The amplitudes of P waves, however, are strongly affected by the properties of the damaged zones and invaded zones. The inclusion of a rigid tool makes the model more real but it is important to understand the effects of its presence when analyzing seismograms.

Thesis Supervisor: M.N. Toksöz

Title: Professor of Geophysics

A Mariella "mi chiquita"
A mis padres "los chiquillos"

ACKNOWLEDGEMENTS

I am grateful to the faculty, staff and students of the M.I.T. Earth Resources Laboratory. In particular, I would like to thank my advisor, Prof. M. N. Toksöz, for his support and assistance which made it possible for me to work at E.R.L.

I will never forget the help, encouragement and friendship given by Arthur "R2D2" Cheng, and the "world famous synthetic microseismograms"; Ralph Stephen introduced me to the most expensive random number generation program and the "roach motel" boundaries; Peter Molnar showed me the other side of the coin, talking to me about magnetic anomalies, gravity and plate tectonics. "Don't leave home without it, especially before Generals!"

During my stay at M.I.T. I made good friends, some of them at the E.R.L. others at the Green building, to all of them my THANKS. Among them I should like to single out Kiyoshi Yomogida (all you have heard about him is true); Rafael Benites (and endless hours of talking about Peru, Peru, and Peru); Gerardo Suarez (the "peruvian" mexican), Hélène Lyon-Caen, and Kaye "pasa" Shedlock my seventh floor mates.

Wafik "Wafico" Beydoun, the best sport coach you'll ever find and Tim Keho ("let's talk about sports nobody else does in the lab!"); introduced me to the fast break and dynamite in Basketball. Ken Tubman and I spent our last summer nights discussing waves, how to beat and cheat in rogue, PCs, thesis font size, and some of the models presented here; and, Carol Blackway, who patiently improved my UNIX and tennis skills.

Karl Coyner, Scott Phillips, COLLEEN BARTON, Michael Prange,Bob Nowack, Jeanne Sauber, John Nabelek, Zhang Jinzhong, Carol Blackway, Jane Maloof, Cengiz

Esmersoy and Rob Stewart contributed greatly to my education and to the exciting experience of being a graduate student at the M.I.T..

Finally, and most importantly, I want to thank Mariella, my wife, for all the big and little efforts that she made in order to cope with this, not always pleasant, period of our life.

TABLE OF CONTENTS

1. INTRODUCTION

For measuring formation parameters such as velocity, density and attenuation in wells we use different logging tools. The sonic logging tool has been used widely to measure formation P velocity. More recently scientists became interested in the full waveform which provides information about the shear wave velocity and other parameters such as attenuation. To obtain the best possible interpretation of an acoustic log, it is necessary to fully understand the physics of elastic wave propagation in and around the borehole. To overcome the mathematical complexity, it is generally assumed that the borehole is an ideal cylinder with axial symmetry and depth independent elastic properties (e.g., Biot, 1952; White and Zechman, 1968; Tsang and Rader, 1979; Cheng and Toksöz, 1981). This type of approach is applicable to idealized geometries and general aspects of wave propagation. The next step in this problem is to gain some insight into the effects of more complicated conditions often encountered in boreholes. For example, it is important to know how a variable borehole diameter between source and receiver affects the logs, and how thin layers and horizontal bed boundaries change the observed waveforms.

At the present time, finite difference or finite element are the only methods, that can be applied to the elastic wave equation, with the potential to answer these questions. In this thesis we describe a finite difference technique for the elastic wave propagation in a borehole and we apply it to investigate effects of borehole complexities on full waveform acoustic logs. In Chapter 2 we present the basic equations used in the finite difference method, and analyze effects which may arise by the misuse, or lack of care, in the implementation of the finite difference method.

Chapter 3 we apply the finite difference method to the acoustic logging problem in simple as well as layered boreholes to investigate the effects of an invaded zone, and the inclusion of a rigid tool. An important aspect of theses studies is to determine

the "depth of investigation" of acoustic logs. The finite difference method shows by snapshots the penetration of wavefront geometries and energy into the formation. Finally, Chapter 4 consists of the discussion and conclusions.

In the Appendices we present detailed mathematical formulations for the liquid-solid interface, the rigid tool, and a description of the sources used in the finite difference modelling.

2. THEORETICAL DEVELOPMENT

Seismic wave propagation in a borehole has been treated by many authors assuming axial symmetry and depth independent properties; in this thesis we will maintain the assumption of axial symmetry. However, we are able to include some depth dependent properties such as washouts, fissures, or horizontal beds in applications. The main goal of this thesis is to test the range of validity of the finite difference method itself.

2.1 The finite difference method

The finite difference method offers a direct and straightforward numerical approach to solve the wave equation with initial and boundary conditions. The method is general and flexible, and may be applied to an inhomogeneous body of any shape. In practice it is necessary to introduce artificial boundaries in order to reduce the model to a finite size. Reducing the effects of artificial boundaries is an important aspect of finite difference modelling.

The size and complexity of a problem that can be solved by the finite difference method is limited by the capability of the available computer. In general, it is necessary to find an algorithm, or a scheme, that minimizes required memory size and computer time. An efficient algorithm must be based upon the maximum symmetry exploitation of a given problem, and the simplification of basic equations and boundary conditions required for accuracy, as well as optimal choices of grid configurations, finite differences formulas and conditions at the artificial or absorbing boundaries.

The finite difference method is essentially an approximation to derivatives. By using

this approximation we are able to solve any differential equation within an error margin. For an example we will use the simple finite difference approximations for a function $\varphi(x)$ which can be expanded in a Taylor series.

$$\varphi(x \pm \Delta x)=\varphi(x) \pm \frac{\partial \varphi}{\partial x}\Delta x + \frac{1}{2}\frac{\partial^2 \varphi}{\partial^2 x}(\Delta x)^2 \pm \frac{1}{6}\frac{\partial^3 \varphi}{\partial^3 x}(\Delta x)^3 + O(\Delta x)^4 \qquad (1)$$

The forward difference approximation is defined by

$$\frac{\partial \varphi^+}{\partial x} \approx \frac{1}{\Delta x}[\varphi(x+\Delta x)-\varphi(x)] \qquad (2)$$

and the backward difference approximation formula by

$$\frac{\partial \varphi^-}{\partial x} \approx \frac{1}{\Delta x}[\varphi(x)-\varphi(x-\Delta x)]. \qquad (3)$$

The truncation error for both cases has a leading term proportional to Δx. On the other hand, if we include more terms, we obtain the central difference approximation formula, defined by

$$\frac{\partial \varphi}{\partial x} \approx \frac{1}{2\Delta x}[\varphi(x+\Delta x)-\varphi(x-\Delta x)]. \qquad (4)$$

with a leading error of order $(\Delta x)^2$.

By adding the Taylor series for $\varphi(x+\Delta x)$ and $\varphi(x-\Delta x)$, we find an approximation formula for $\partial \varphi^2 / \partial x^2$:

$$\frac{\partial^2 \varphi}{\partial^2 x} \approx \frac{1}{(\Delta x)^2}[\varphi(x+\Delta x)-2\varphi(x)+\varphi(x-\Delta x)]. \qquad (5)$$

The leading term of this approximation formula is also of second order [$(\Delta x)^2$]. Abramowitz and Stegun [1965] present formulas with higher order approximations. These schemes were first used by Alterman and Karal [1968] and Ottaviani [1971], but in both cases they solved a homogeneous explicit case.

A list of all the papers on the finite difference method in seismology would be too

lengthy to include here. Three papers were "pioneers" in the work: Alterman and Karal [1968]; Boore [1972]; and Kelly et al. [1976].

2.2 The elastic wave equation solution

The wave equation in seismology has been solved by many different approaches. A good review of all the methods appeared in a paper by Chin *et al.* [1982]. The principal goal is to calculate synthetic seismograms that will allow us to better understand the forward problem and to hopefully solve the inverse problem.

Finite difference and finite element are powerful methods of obtaining synthetic seismograms for complicated geometries as well as for simpler cases. However, the computation of the high-frequency response becomes expensive because of the need for smaller meshes. These are known to be useful in a case of a laterally heterogeneous medium, because the amount of computation is not necessarily dependent on the geometrical complexity.

The equation to be solved is the elastic wave equation for perfectly elastic, isotropic media in the absence of body forces (Aki and Richards, 1980):

$$\rho \ddot{u}_i = \tau_{ij,j} \tag{6}$$

where ρ is density, u_i is the displacement vector and $\ddot{u}_i$ is the acceleration vector. τ_{ij} is the stress tensor for isotropic media, with summation over repeated indices. The stress tensor for isotropic media can be written as

$$\tau_{ij} = [\lambda \delta_{ij} \delta_{kl} + \mu(\delta_{ik}\delta_{jl} + \delta_{il}\delta_{jk})] e_{kl} \tag{7}$$

where λ and μ are Lame's parameters, δ_{ij} is the Kronecker delta, and $e_{kl} = \frac{1}{2}(u_{k,l} + u_{l,k})$ is the strain tensor. Equation (6) is solved in two-dimensional cylindrical co-ordinates (r,z) and the parameters (ρ,λ,μ) are assumed to be

functions of radius r and depth z only. In the case of a borehole without a rigid tool, a compressional point source is located in the liquid on the axis of symmetry ($r=0$) and a liquid-solid interface is located at a radius, R. With a rigid tool, a compressional source is located on the rigid tool wall and can be viewed as a ring around the tool. A vertical line of pressure receivers will be located below the point source on the axis of symmetry (Figure 1) or along the surface of the rigid tool (Figure 2). The time dependence of the source pressure function is shown in Appendix A3.

As outlined by Alterman and Loewenthal [1972] and Kelly *et al.* [1976], the elastic wave equation with the parameters (ρ,λ,μ), (functions of radius and/or depth) can be solved directly using an explicit finite difference method. In terms of displacements, equations (6) and (7) become

$$\rho\ddot{\vec{u}}=(\lambda+\mu)\nabla(\nabla\cdot\vec{u})+\mu\nabla^2\vec{u}+\nabla\lambda(\nabla\cdot\vec{u})+\nabla\mu\times(\nabla\times\vec{u})+2(\nabla\mu\cdot\nabla)\vec{u} \tag{8}$$

The finite difference formulation of this equation in cylindrical coordinates in a heterogeneous media is given by Stephen [1983].

Assuming isotropy and homogeneity, we can express the vector equation (8) by two scalar equations for the horizontal and vertical displacements.

$$\rho u_{tt}-(\lambda+2\mu)(u_{rr}+\frac{1}{r}u_r-\frac{1}{r^2}u)-\mu u_{zz}-(\lambda+\mu)w_{rz}=0 \tag{9}$$

$$\rho w_{tt}-\mu(w_{rr}+\frac{1}{r}w_r)-(\lambda+2\mu)w_{zz}-(\lambda+\mu)(u_{rz}+\frac{1}{r}u_z)=0 \tag{10}$$

This formulation is useful and faster if we solve the wave equation in a fluid and a solid with homogeneous properties. Between both materials we have to include either an interface, in order to satisfy the boundary conditions, or an interface and a transition zone. The finite difference solutions using equations (9) and (10) are given

in Appendices A and B.

2.3 Constraints, limitations and accuracy

The principal cause of inaccuracy in finite difference calculations for slowly varying media is grid dispersion. If the grid increments $(\Delta r, \Delta z)$ are too large, low frequencies will travel faster across the grid than high frequencies, causing apparent dispersion. This result is generally true for compressional waves. For shear waves the dispersion relation is more complex and for some combinations of Poisson's ratio and propagation direction high frequencies will travel faster than low frequencies [Bamberger *et al*, 1980].

To better understand this effect we look at a simple function

$$\varphi(t) = e^{i\omega t} \tag{11}$$

and

$$\frac{\partial^2 \varphi(t)}{\partial t^2} = -\omega^2 \varphi(t) \tag{12}$$

Using the approximation formula we obtain

$$\frac{\partial^2 \varphi(t)}{\partial t^2} \approx \frac{e^{-i\omega\Delta t} - 2e^0 + e^{i\omega\Delta t}}{(\Delta t)^2} \varphi(t) \tag{13}$$

which can be simplified into

$$\frac{\partial^2 \varphi(t)}{\partial t^2} \approx \frac{2\cos\omega\Delta t - 2}{(\Delta t)^2} \varphi(t) = -\frac{4}{(\Delta t)^2} \sin^2\left(\frac{\omega\Delta t}{2}\right) \varphi(t) = -\hat{\omega}^2 \varphi(t) \tag{14}$$

From equation (14) we can observe that the finite difference method uses an apparent value $\hat{\omega}$ for the frequency ω.

$$\hat{\omega} = \frac{2}{\Delta t} \sin\left(\frac{\omega\Delta t}{2}\right) \approx \frac{2\omega\Delta t}{2\Delta t} = \omega \tag{15}$$

The approximation holds when $\omega\Delta t$ is small. For high frequencies the apparent frequency $\hat{\omega}$ becomes significantly smaller than the true value ω . For a fixed wavenumber this implies a slower phase velocity.

Trefethen [1982] found that energy travels faster at 45 ° and slower in any other direction. An analysis for a general finite difference calculation has been made by Sato and Ishihara [1983], yielding similar results. Compressional waves are slower at high frequencies; shear waves are faster at high frequencies and generally at angles closer to 45 ° , because they are undersampled. The dispersion is also dependent on the ratio $\frac{\lambda}{\mu}$; the closer to 1 this ratio (Poisson ratio equal to 0.25), the smaller will be the dispersion.

To investigate effects of grid size we use the acoustic wave equation in cartesian coordinates.

$$\frac{1}{v^2}\frac{\partial^2 u}{\partial t^2} = \frac{\partial^2 u}{\partial x^2} + \frac{\partial^2 u}{\partial y^2} \tag{16}$$

Applying a tridimensional Fourier Transform we obtain

$$-\frac{\omega^2}{v^2} = -k_x^2 - k_z^2 \tag{17}$$

the finite difference approximation is

$$-\frac{4}{(v\Delta t)^2}\sin^2\left(\frac{\omega\Delta t}{2}\right) = -\frac{4}{(\Delta x)^2}\sin^2\left(\frac{k_x\Delta x}{2}\right) - \frac{4}{(\Delta y)^2}\sin^2\left(\frac{k_y\Delta y}{2}\right) \tag{18}$$

or more simply

$$\sin^2\left(\frac{\omega\Delta t}{2}\right) = v^2\frac{(\Delta t)^2}{(\Delta x)^2}\left[\sin^2\left(\frac{k_x\Delta x}{2}\right) + \frac{(\Delta x)^2}{(\Delta y)^2}\sin^2\left(\frac{k_y\Delta y}{2}\right)\right] \tag{19}$$

If we define $\Delta x = \Delta y$, we then obtain the stability condition for a homogeneous two dimensional acoustic case $\Delta t \leq \frac{1}{\sqrt{2}}\frac{\Delta x}{v}$.

The grid size in this finite difference model is defined by using the following formula:

$$\Delta x = \frac{V_{min}}{n f_{max}} \tag{20}$$

where the factor n represents the number of points per wavelength to be used, f_{max} the maximum frequency, and V_{min} the minimum velocity value in all of the model.

In the case of propagation in infinite elastic homogeneous media, explicit finite difference formulation is stable only if:

$$\Delta t \leq \frac{\min(\Delta r, \Delta z)}{\sqrt{\alpha^2+\beta^2}} \tag{21}$$

where $\alpha = \sqrt{\frac{\lambda+2\mu}{\rho}}$, $\beta = \sqrt{\frac{\mu}{\rho}}$, Δr and Δz represent the grid size in the radial and depth axis, and Δt is the time step necessary to calculate the time derivative accurately. Kelly *et al.* [1976] suggested that stability in heterogeneous media could be expected provided equation (21) held everywhere on the grid. This is only valid for the case of "slowly" varying media. Unfortunately, sharp interfaces treated with the heterogeneous formulation do not satisfy this condition. The method becomes unstable at such interfaces.

Estimates of the number of grid points per wavelength, which will give acceptable results, vary from ten to thirty. This uncertainty makes the comparison of finite difference results with results of other techniques extremely important.

In order to minimize the computation time, it is necessary to minimize the number of grid points. This is accomplished by the proper selection of axes of symmetry and absorbing boundaries. In the present model the top and left-hand boundaries are selected to be the axes of symmetry, thus placing the compressional point source in the upper left corner (see Figures 1 and 2). An exact finite difference formulation of

the elastic wave equation is possible at axes of symmetry and these are generally preferable to absorbing boundaries where approximations must be made. The axes of symmetry formulation can be obtained from the formulation outlined in equations (9) and (10) by either applying symmetry conditions for the displacements or applying l'Hospital's rule for terms containing $1/r$, (e.g., for the left-hand boundary, $\frac{1}{r}\frac{\partial u}{\partial z}$ becomes $\frac{\partial^2 u}{\partial r\,\partial z}$ as r goes to zero) [Alterman and Loewenthal, 1972].

The different types of models to be used in this paper are presented in Figure 3 with the density and velocity values of the fluid and the formation. For the absorbing boundaries we follow the formulation of Clayton and Engquist [1977], corrected by Fuyuki and Matsumoto [1980] and modified by Emerman and Stephen [1983]. The method assumes a parabolic approximation to the elastic wave equation about an axis normal to the boundary and works best for energy propagating at near normal incidence. We also follow the formulation of Reynolds [1978] in the lower boundary (z = constant); this formulation is more accurate than the previous one in heterogeneous cases. The Reynolds method assumes a special boundary condition and wave equation that allows only one-way propagation, which works best for energy propagating at near normal incidence.

Guided waves are not absorbed by boundary conditions based on the parabolic approximation [Fuyuki and Matsumoto, 1980]. The component of displacement parallel to the boundary of the elliptical particle motion of the guided waves causes problems if the boundary is close to the borehole. To avoid this problem a minimum of two wavelengths of the lowest frequency guided wave was used as a criterion for the placement of the grid boundary away from the liquid-solid sharp interface.

In the case of a soft formation, because of the long period (large wavelength) of the Stoneley wave and the considerable amount of energy traveling on it, the location of

the absorbing boundaries has to be pushed away from the center of the borehole as opposed to the cases analyzed in this thesis. This increase makes it almost impossible to model large offsets. In order to obtain accurate far offset cases, therefore, it is imperative to develop an improved absorbing boundary schema.

3. APPLICATIONS TO BOREHOLES

We present applications of the finite difference method using an open hole or a rigid tool, a liquid-solid sharp interface or a liquid-solid sharp interface plus an invaded zone.

3.1 Seismic waves in a fluid filled borehole

In order to better understand the wave propagation problem in a fluid filled borehole it is important to recognize the importance of the geometry of the borehole and the different type of waves belonging to it.

The basic geometry of the problem is presented in Figure 1 where we have a cylindrical hole drilled within the formation and filled with a fluid (mud). For the simplest case we have a two media problem: the mud and the formation. During the process of drilling, the formation surrounding the bore may be modified (i.e. damaged and/or invaded by the mud). In this case the problem will have an intermediate layer with properties varying from the fluid solid interface to the virgin formation. Several authors have worked on analytical solutions of the wave propagation problem; Biot [1952], Somers [1953], White [1962] and Peterson [1974] investigated the dispersion characteristic of the guided waves in a solid borehole while Jacobi [1949] investigated the case of a two cylindrical fluid media. More recently the inclusion of a logging tool has been made by Wyatt [1979], and Cheng and Toksõz [1980,1981].

Synthetic seismograms for a fluid filled borehole have been calculated by White [1967]; White and Zechman [1968]; Rosenbaum [1974]; Tsang and Rader [1979]; Cheng and Toksöz [1980,1981]; and Paillet and White [1982]. Cylindrical layered

models have been treated by Schoenberg et al. [1981]; Chang and Everhart [1983]; Baker [1984] and Tubman et al. [1984].

We will analyze the case of $V_p > V_s > V_f$, symbols that correspond to the formation compressional velocity, formation shear velocity and fluid velocity. An example of a full waveform seismogram is shown in Figure 3.

The first wave is the P wave which corresponds to a compressional wave in the fluid, critically refracted into the formation as a compressional wave and refracted back into the fluid as a compressional wave (PPP). The second wave to be observed is the S wave which corresponds to a compressional wave in the fluid, critically refracted into the formation as a shear wave and refracted back into the fluid as a compressional wave (PSP). Both waves behave as head waves when they reach the formation.

In addition there are guided waves. One group of guided waves is called reflected conical waves by Biot [1952], normal modes by Tsang and Rader [1979] or pseudo Rayleigh waves by Cheng and Toksöz [1980,1981]. The main property of these waves is that in the formation they decay radially away from the borehole and that they are oscillatory in the fluid. These waves are dispersive, and Figure 4 shows the dispersion curves from Cheng and Toksöz [1981]. The velocities have been normalized by the fluid velocity, both the phase and group velocities have an upper bound equal to the shear velocity of the formation. The minimum value for the phase velocity is equal to the compressional wave velocity of the fluid. The group velocity has a slightly more complicated pattern, having a minimum value below the fluid compressional wave velocity, region that will explain the Airy phase, but at high frequency the group velocity reaches the value of the fluid compressional wave velocity asymptotically. The dispersion curve explains why the arrival of the pseudo Rayleigh wave is spread in time, starting with the arrival of the S wave (

corresponding to the low frequency cutoff [a] in Figure 3), and finishing with the Airy phase ([c] in Figure 3).

Between sections [a] and [c] in Figure 3 there is a strong low frequency arrival noted as [b] that corresponds to the Stoneley wave. This wave travels almost without dispersion at a speed slightly slower than the fluid velocity. The amplitude of this pulse decays exponentially away from the borehole wall, both in the fluid and the formation, a property that will later help us to identify it in the snapshots.

3.2 The Liquid-Solid interface

To check the results from the finite difference method (FD), it is necessary to compare them with results from a well established technique like the discrete wavenumber summation method (DW) (Bouchon and Aki, 1977; Cheng and Toksöz, 1981). For the comparison we will use the simple model where the borehole is in a homogeneous formation.

In this case the solution of the wave equation in the solid and in the liquid is related to the following boundary conditions:

a) the continuity of the stress normal to the borehole wall,

b) the disappearance of the tangential stress in the solid,

c) the continuity of the normal displacement.

Additionally, we note that the vertical displacement in the borehole wall is discontinuous.

In order to compare the finite difference and discrete wavenumber approaches for liquid-solid interfaces, it is necessary to specifically code the boundary conditions for the sharp interface [Stephen 1983]. A second order approximation in the space increments gives the best results. Stephen compared the results of the finite difference formulation for a sharp liquid-solid interface to the reflectivity method for sea floor models. In this paper, the second-order formulation for a sharp liquid-solid cylindrical borehole interface, as well as the second-order formulation for a cylindrical rigid tool-liquid interface, are given (Appendices A1 and A2). Different synthetic seismograms are calculated to illustrate effects of grid size, dispersion and formation properties on finite difference solutions. Model parameters used are tabulated in Figure 5.

In Figure 6 the synthetic seismograms calculated by the discrete wavenumber method (6a) and finite difference method (6b) are compared. The formation and fluid properties are those of Model 1 in Figure 5. The radius of the borehole is 0.1m and the center frequency of the source is 15 kHz with a bandwidth of 5 kHz. In the synthetic seismogram calculated using the finite difference method, 15 points per wavelength at the highest frequency, are used for the compressional wave. There is a very close match of the two waveforms; the P wave trains are almost identical, the S wave arrivals are well matched, and there is good agreement between the two seismograms, including the pseudo-Rayleigh and Stoneley wave packet. There are some phase differences in the two seismograms in the guided wave packet. At the tail end of the FD seismogram there is some ringing which is absent from the DW seismogram. In general, the overall agreement between the two methods is quite good. A reduction of the time step by a factor of 2 doesn't improve the solution as expected. Equation (21) has to be used carefully, and the better selection for Δt is equal to the maximum value possible. This selection will imply the smaller induced numerical dispersion.

In Figure 7, the center frequency of the source is reduced to 10.6 kHz. There is an excellent match between the two seismograms. The only difference is a slight arrival time difference in the Stoneley wave pulse at about 1.35 msec. Again we used 15 points per wavelength and the Model 1 (Figure 5).

It is clear from Figures 6 and 7 that the frequency content of the signal is very important in the generation of the synthetic seismogram. The frequency content affects the choice of both the grid size and the time step in the FD solution. The time step Δt is related to the grid size Δx through equation (21), and the grid size is defined by:

$$\Delta x = \frac{V_{min}}{10 f_{max}} \tag{22}$$

The factor 10 in the denominator represents the minimum allowable number of grid points per wavelength of the shortest wavelength body wave. Unless otherwise indicated, we normally used 10 points per wavelength. In the case of a fluid filled borehole one must deal not only with P and S wave velocities, but also pseudo-Rayleigh and Stoneley waves, which propagate with velocities lower than the fluid velocity. A factor of 0.8 was used to reduce the smallest velocity in the system (α_f or β) for the grid size calculations. Due to dispersion in the guided waves, the calculated value of Δx is smaller than that required for almost every frequency, implying that the value of Δt is also smaller than the minimum required. Thus, the slower the wave, the bigger the induced dispersion in comparison to faster waves.

Another consideration in the borehole problem is the maximum frequency, f_{max}, used in equation (22). Normally f_{max} is taken to be the upper-half-power frequency of the source. In the borehole case, however, this frequency is not always adequate. Figure 8a shows the frequency spectrum of the DW synthetic seismogram shown in

Figure 6a. Although the source used in Figure 6 has an upper-half-power frequency of 20 kHz, there is significant energy at about 23 kHz. This is due to the excitation of the second mode of the pseudo-Rayleigh wave (Cheng and Toksöz, 1981; Paillet, 1980). The grid size used to calculate the waveform in Figure 6b gives a number of grid points per wavelength which is less than 10 in that case. This is reflected in the phase difference in the pseudo-Rayleigh wave packets between the FD and DW synthetic seismograms shown in Figure 6. For comparison, the frequency spectrum for the DW synthetic in Figure 7a is shown in Figure 8b. The higher mode of the pseudo-Rayleigh wave is clearly not excited at this lower frequency, and the grid spacing used is adequate.

3.3 Inclusion of a Rigid Tool

In this case the solution of the wave equation in the rigid tool and in the liquid is related to the following boundary conditions:

a) the continuity of the stress normal to the borehole wall,

b) the vanishing of the tangential stress in the rigid tool,

c) the vanishing of the normal displacement.

In order to compare seismograms with and without the rigid tool in the borehole, we start with an open hole seismogram. Figures 9 and 10 show open hole results for formation parameters of Model 2 (Figure 5). Figure 9 is obtained with the finite difference method and Figure 10 is generated with the discrete wavenumber method. The center frequency is 12 Khz, and the bandwidth is 4 Khz. The match is good but

not perfect, the P and S comparison is good, but the match of Rayleigh and Stoneley wave packets is degraded, primarily because the presence of the second mode of the pseudo Rayleigh wave affects the number of grid points per wavelength.

Figures 11 and 12 illustrate the case of the inclusion of a rigid tool of 4.5cm radius (Model 2, Figure 5). Note the increased number of cycles before the S arrival. In general, the P waveforms in the rigid tool case show more oscillations than the open hole case with the same borehole radius. This is an expected observation. The match between methods is surprisingly good, though again the last part of the waveform presents some problems. But in this case the pseudo-Rayleigh wave dispersion curves are shifted to higher frequencies (Cheng and Toksöz 1981). The second mode of the Rayleigh wave is not excited and the number of grid points per wavelength is adequate. This shows the importance of the influence of the different modes of the guided waves and the care one must take in the generation of the finite difference synthetics.

These examples show that where there are a number of wave types propagating with different velocities, finite difference grid parameters cannot be the optimum for each and every wave. As a result a choice has to be made. This is acceptable as long as the limitations and effects are understood. Comparison with discrete wavenumber results was helpful in establishing the limitations of finite difference.

3.4 Existence of a Damaged Zone

The drilling process may damage the formation immediately around the borehole. The damaged zone thickness could be equal to the borehole radius. Long-spaced full waveform acoustic logs may be able to "see" past the altered zone and measure the true formation properties. To verify this we have studied the depth of investigation

of refracted body waves in an altered borehole using both the ray theory and the finite difference approach. We calculated the minimum source-receiver separation necessary to observe the unaltered formation and we found that it depended on both the velocity gradient and the extent of the altered zone. However, it is not clear that the ray theory is valid in this case because of the comparable size of the wavelength, the borehole radius and the thickness of the altered zone.

A velocity model for a borehole with an altered zone is shown in Figure 13. Reduced velocities represent the damaged zone. The model has a liquid-solid sharp interface with a varying velocity zone between the interface and the unaltered formation. The shaded area represents the range of possible shear wave velocity values that this layer may have. This situation happens mainly when the effective pressure on the rock skeleton diminishes because of the increase of the pore pressure.

In order to better understand the phenomena, rays traced across the linear velocity gradient zone are shown (Figure 14). We observe that if the thickness of the damaged zone increases, the ability to observe a ray coming back from the unaltered formation is reduced. If we increase the formation velocity without changing the geometry, the source-receiver separation necessary to see the rays refracted from the formation is also reduced (Figure 15).

The minimum source-receiver separation that will permit us to observe the properties of the formation through the altered zone can be calculated using ray theory:

$$z = 2D\left[\frac{v_1 + v_0}{v_1 - v_0}\right]^{1/2} + 2R\,\frac{v_f}{(v_1^2 - v_f^2)^{1/2}} \tag{23}$$

where z is the value for the minimum source-receiver separation required to "see" the unaltered formation in an open borehole with an invaded zone of thickness D

and with a positive linear velocity gradient. Using equation (23) we generated the Table presented in Figure 16 with different values of velocity and thickness of the damaged zone.

Synthetic seismograms generated with the finite difference method in a borehole with and without a rigid tool, and with a damaged zone surrounding the borehole, are presented in Figures 17 and 18 respectively, using Model 3 (Figure 5). Compared with the homogeneous formation case in Figure 9, we observe a small travel time delay in the damaged zone case, and an increment in the P wave amplitude (Figure 17). This amplitude increase is due to more energy with a ray parameter close to the critical value being channeled through the damaged zone. The decay with distance z is smaller than that of a head wave.

Figure 18 presents a damaged zone case with a rigid tool using Model 3 (Figure 5). It is hard to see a big difference between Figure 11 and Figure 18 . The main difference is the amplitude increase of the P wave and also a small amplitude increase in the S and Rayleigh waves, but the observations are too close to the source for this difference to be obvious. The additional beating observed at the end of the traces is due to the reflections from the absorbing boundary. In the rigid tool case more energy is generated in the radial direction, and the reflection effect becomes important. In Figure 19 we compared the travel times picked from the finite difference synthetic seismograms and calculated by ray theory using parameters given in Model 4 (Figure 5). The agreement is good beyond the critical distance.

Finally, in Figures 20 and 21 we present record sections for Model 3 (Figure 5) in an open hole and a hole with a rigid tool. The size of the damaged zone is 9cm. The minimum source-receiver separation calculated using Eq. (23) gives us a value of 90cm for the open hole case and 85cm for the rigid tool case. In the figures these values can be related to the decrease in amplitudes of the P waves at the point where

the transition from the rays being bent back by the velocity gradient to the rays refracted along the unaltered formation occurs (Figures 17 and 18).

In Figures 22 and 23 we present the "snapshots" of the two previous record sections. The differences between the cases with and without a rigid tool in an open borehole are clear and can be identified as higher frequency in the Rayleigh wave packet in the rigid tool case. More reverberations and wave trains are seen in the solid because the existence of the rigid tool makes a thinner liquid layer. At 18cm from the center of the borehole, there where the virgin formation starts, we can also identify the beginning of the wavefronts propagating at the highest possible speed.

3.5 Existence of an Invaded or Flushed Zone

Drilling fluid invading the formation can increase or decrease velocities depending on whether the formation is brine or gas saturated. In Figure 24 we show a typical velocity profile for an invaded zone in a gas saturated formation. Compressional wave velocity is increased due to fluid invasion but shear velocity remains nearly constant (Johnston 1978). The Models 5, 6, 7 and 8 (Figure 5) represent a series of invaded models.

In Figure 25 we present a record section corresponding to Model 6 (Figure 5); the velocity calculated from the record section is constant and equal to 3.93 Km/sec. The velocity of the flushed zone is 4.13 Km/sec and the velocity of the virgin formation is 4.00 Km/sec. The amplitudes of the P wave arrivals are smaller than in a similar damaged zone (Figure 26 Model 9) case.

In Figure 27 we present a similar record section, but this time from Model 5 (Figure 5). This model is similar to Model 6 except for the size of the flushed zone (9cm vs.

27 cm). We do not see a major difference between seismograms in Figures 25 and 27 in spite of the big change in the size of the flushed zone (300%). The P wave velocity measure in Figure 27 is 3.90 Km/sec. To investigate this phenomenon further we increased the contrast to 14% (Models 7 and 8), compared to 3% of Models 5 and 6.

Figures 28 and 29 show the record sections corresponding to Models 8 and 7 respectively. The speed of the P wave obtained in the short flushed zone case to 3.70 Km/sec and in the large flushed zone case is equal to 3.75 Km/sec.

This method cannot better accuracy because it has a major grid dispersion problem which cannot as yet be so controlled as to obtain the correct velocity values. We have seen two different cases, however, where the P wave velocity was determined by measuring the travel time slope, and the results were not clear enough to establish the absence of a flushed zone.

We can conclude that for large offsets the P wave velocity will tend to the virgin formation value, as in the case of the damaged zone. In Figure 30 we present the record section for the damaged zone case (Model 3 in Figure 5). We can observe that the basic difference between the previous record sections is the amplitude of the P wave train. Moreover, seismograms do not differentiate a damaged zone from a flushed zone. The amplitude difference results from the focusing effect in the case of a damaged zone, and from a change in Poisson's ratio in case of damage and/or invasion. The P wave velocity measured in this case is 3.93 Km/sec

For a final comparison, Figure 31 presents the record section for Model 8 (Figure 5) in the same format as Figure 11. The differences between these two figures (11 and 31) are too small to be observable.

CONCLUSIONS

Synthetic acoustic logs which demonstrate the salient features of observed logs can be generated by the finite difference method using appropriate formulations. A comparison between the discrete wavenumber method and the finite difference method showed that the latter should be used carefully in the interpretation of the synthetic seismograms, especially in the case of guided waves. The use of a heterogeneous formulation in a borehole with a damaged zone allows us to compare the model velocities with velocities determined from theoretical record sections. This comparison shows that it is necessary to have a large source-receiver spacing in order to "see" past the damaged zone.

Models calculated for invaded or flushed zones show the effects of invasion on full waveforms. Generally the effect on velocities is small. The amplitudes of P waves, however, are strongly affected by the properties of the damaged zones and invaded zones.

The inclusion of a rigid tool affects the character of seismograms. It is important to understand the effects of the tool properties when comparing theoretical and observed seismograms.

APPENDIX

A1. Second Order Boundary Conditions for a Liquid-Solid Cylindrical Interface

It is necessary to formulate the liquid-solid interface specifically in the finite difference code by boundary conditions [Stephen, 1983]. That formulation was made for interfaces normal to the depth z axis and is inappropriate for interfaces normal to the radius r in cylindrical co-ordinates. The formulation for this case, which is analogous to a formulation for solid-solid interfaces originally presented by Ungar and Ilan [1977], is given below.

The wave equation in the homogeneous liquid to the left of the interface (see Figure 1) is:

$$\rho_1 u_{tt}^1 - \lambda_1 (u_{rr}^1 + \frac{1}{r} u_r^1 - \frac{1}{r^2} u^1) - \lambda_1 w_{rz}^1 = 0 \tag{A1-1}$$

$$\rho_1 w_{tt}^1 - \lambda_1 (u_{rz}^1 + \frac{1}{r} u_z^1) - \lambda_1 w_{zz}^1 = 0 \tag{A1-2}$$

and in the homogeneous solid to the right of the interface:

$$\rho_2 u_{tt}^2 - (\lambda_2 + 2\mu_2)(u_{rr}^2 + \frac{1}{r} u_r^2 - \frac{1}{r^2} u^2) - \mu_2 u_{zz}^2 - (\lambda_2 + \mu_2) w_{rz}^2 = 0 \tag{A1-3}$$

$$\rho_2 w_{tt}^2 - \mu_2 (w_{rr}^2 + \frac{1}{r} w_r^2) - (\lambda_2 + 2\mu_2) w_{zz}^2 - (\lambda_2 + \mu_2)(u_{rz}^2 + \frac{1}{r} u_z^2) = 0 \tag{A1-4}$$

The boundary conditions, which must hold at the liquid-solid interface, are a continuity of normal stress,

$$\lambda_1 (u_r^1 + \frac{1}{r} u^1) + \lambda_1 w_z^1 = (\lambda_2 + 2\mu_2) u_r^2 + \lambda_2 (\frac{1}{r} u^2 + w_z^2), \tag{A1-5}$$

a vanishing of the tangential stress in the solid,

$$\mu_2 (u_z^2 + w_r^2) = 0, \tag{A1-6}$$

and a continuity of normal displacement,

$$u^1=u^2. \tag{A1-7}$$

The superscripts, 1 and 2, refer to values in the liquid and solid respectively. The unknowns in the derivation are the horizontal displacement at the interface, $u^{1,2}(M,n,l)$, the vertical displacement in the liquid at the interface, $w^1(M,n,l)$ and the vertical displacement in the solid at the interface, $w^2(M,n,l)$. The interface is at a radius of $R=M\Delta r$.

Additional relationships required in the derivation are the Taylor expansions:

$$-\Delta r u_r^1+\frac{1}{2}\Delta r^2 u_{rr}^1=u^1(M-1,n,l)-u^1(M,n,l) \tag{A1-8}$$

$$\Delta r u_r^2+\frac{1}{2}\Delta r^2 u_{rr}^2=u^2(M+1,n,l)-u^2(M,n,l) \tag{A1-9}$$

$$\Delta r w_r^2+\frac{1}{2}\Delta r^2 w_{rr}^2=w^2(M+1,n,l)-w^2(M,n,l) \tag{A1-10}$$

and the finite difference expressions for mixed derivatives:

$$\begin{aligned}-2\Delta r\,\Delta z w_{rz}^1=&w^1(M-1,n+1,l)-w^1(M-1,n-1,l)\\&-w^1(M,n+1,l)+w^1(M,n-1,l)\end{aligned} \tag{A1-11}$$

$$\begin{aligned}2\Delta r\,\Delta z u_{rz}^2=&u^2(M+1,n+1,l)-u^2(M+1,n-1,l)\\&-u^2(M,n+1,l)+u^2(M,n-1,l)\end{aligned} \tag{A1-12}$$

$$\begin{aligned}2\Delta r\,\Delta z w_{rz}^2=&w^2(M+1,n+1,l)-w^2(M+1,n-1,l)\\&-w^2(M,n+1,l)+w^2(M,n-1,l).\end{aligned} \tag{A1-13}$$

The finite difference formulation for the horizontal displacement on the interface, is obtained by solving equations (A1-1), (A1-3), (A1-5), (A1-7), (A1-8), (A1-9), (A1-11) and (A1-13), and replacing z and t derivatives with centered finite differences. Hence:

$$
\begin{aligned}
u^{1,2}(M,n,l+1)=&2u^{1,2}(M,n,l)-u^{1,2}(M,n,l-1)\\
&+a_1[w^2(M,n+1,l)-w^2(M,n-1,l)]\\
&+a_2[w^1(M,n+1,l)-w^1(M,n-1,l)]\\
&+a_3u^{1,2}(M,n,l)\\
&+a_4[u^2(M+1,n,l)-u^{1,2}(M,n,l)]\\
&+a_5[u^{1,2}(M,n,l)-u^1(M-1,n,l)]\\
&+a_6[u^{1,2}(M,n+1,l)-2u^{1,2}(M,n,l)+u^{1,2}(M,n-1,l)]\\
&+a_7[w^2(M+1,n+1,l)-w^2(M,n+1,l)-w^2(M+1,n-1,l)+w^2(M,n-1,l)]\\
&+a_8[w^1(M,n+1,l)-w^1(M-1,n+1,l)-w^1(M,n-1,l)+w^1(M-1,n-1,l)]
\end{aligned}
$$

where

$$a_1=\frac{\Delta t^2}{\Delta r\Delta z}\frac{\lambda_2}{(\rho_1+\rho_2)}$$

$$a_2=-\frac{\Delta t^2}{\Delta r\Delta z}\frac{\lambda_1}{(\rho_1+\rho_2)}$$

$$a_3=\frac{\Delta t^2}{\Delta r^2}\frac{2}{(\rho_1+\rho_2)}\left[\frac{1}{M}(\lambda_2-\lambda_1)-\frac{1}{2M^2}(\lambda_2+2\mu_2+\lambda_1)\right]$$

$$a_4=\frac{\Delta t^2}{\Delta r^2}\frac{2(\lambda_2+2\mu_2)}{(\rho_1+\rho_2)}\left(1+\frac{1}{2M}\right)$$

$$a_5=-\frac{\Delta t^2}{\Delta r^2}\frac{2\lambda_1}{(\rho_1+\rho_2)}\left(1-\frac{1}{2M}\right)$$

$$a_6=\frac{\Delta t^2}{\Delta z^2}\frac{\mu_2}{(\rho_1+\rho_2)}$$

$$a_7=\frac{\Delta t^2}{\Delta r\Delta z}\frac{(\lambda_2+\mu_2)}{2(\rho_1+\rho_2)}$$

$$a_8=\frac{\Delta t^2}{\Delta r\Delta z}\frac{\lambda_1}{2(\rho_1+\rho_2)}$$

In all the formulations presented in this paper $\vec{u}=(u,w);\Delta r,\Delta z,\Delta t$ are the increments in radius, depth and time and m, n, l are the indices for radius, depth and time (i.e. $(m,n,l)=(m\Delta r,n\Delta z,l\Delta t)$).

Similarly, by solving equations (A1-1), (A1-2) and (A1-8) for the vertical displacement in the liquid at the interface one obtains:

$$
\begin{aligned}
w^1(M,n,l+1)=&2w^1(M,n,l)-w^1(M,n,l-1)\\
&+b_1[w^1(M,n+1,l)-2w^1(M,n,l)+w^1(M,n-1,l)]\\
&+b_2[u^1(M,n+1,l)-u^1(M,n-1,l)]\\
&+b_3[u^1(M,n+1,l)-u^1(M-1,n+1,l)-u^1(M,n-1,l)+u^1(M-1,n-1,l)]\\
&+b_4[u^1(M,n+1,l+1)-2u^1(M,n+1,l)+u^1(M,n+1,l-1)\\
&\quad -u^1(M,n-1,l+1)+2u^1(M,n-1,l)-u^1(M,n-1,l-1)]\\
&+b_5[w^1(M,n+1,l)-2w^1(M,n,l)+w^1(M,n-1,l)\\
&\quad -w^1(M-1,n+1,l)+2w^1(M-1,n,l)-w^1(M-1,n-1,l)]\\
&+b_6[u^1(M,n+1,l)-u^1(M,n-1,l)-u^1(M-1,n+1,l)+u^1(M-1,n-1,l)]
\end{aligned}
$$

where

$$b_1=\left(\frac{\Delta t^2}{\Delta z^2}\right)^2\frac{\lambda_1}{\rho_1}$$

$$b_2=\frac{\Delta t^2}{\Delta r\,\Delta z}\frac{\lambda_1}{2\rho_1}\left(\frac{1}{M}+\frac{1}{2M^2}\right)$$

$$b_3=\frac{\Delta t^2}{\Delta r\,\Delta z}\frac{\lambda_1}{2\rho_1}$$

$$b_4=\frac{\Delta r}{4\Delta z}$$

$$b_5=-\frac{\Delta t^2}{\Delta z^2}\frac{\lambda_1}{2\rho_1}$$

$$b_6=-\frac{\Delta t^2}{\Delta z\,\Delta r}\frac{\lambda_1}{\rho_1}\frac{1}{4M.}$$

Note that this solution requires the horizontal component on the interface at future points in time ($(l+1)\Delta t$) and that it must follow the calculation of the horizontal components.

The vertical displacement in the solid at the interface is obtained from equations (A1-4), (A1-6), (A1-10), and (A1-12):

$$
\begin{aligned}
w^2(M,n,l+1) = {} & 2w^2(M,n,l) - w^2(M,n,l-1) \\
& + c_1[u^{1,2}(M,n+1,l) - u^{1,2}(M,n-1,l)] \\
& + c_2[w^2(M+1,n,l) - w^2(M,n,l)] \\
& + c_3[w^2(M,n+1,l) - 2w^2(M,n,l) + w^2(M,n-1,l)] \\
& + c_4[u^2(M+1,n+1,l) - u^2(M,n+1,l) - u^2(M+1,n-1,l) + u^2(M,n-1,l)]
\end{aligned}
$$

where

$$c_1 = \frac{\Delta t^2}{\Delta r \Delta z}\frac{\mu_2}{\rho_2}\left[1 + \frac{1}{2M}\frac{(\lambda_2+\mu_2)}{\mu_2}\right]$$

$$c_2 = \frac{\Delta t^2}{\Delta r^2}\frac{2\mu_2}{\rho_2}\left(1 + \frac{1}{2M}\right)$$

$$c_3 = \frac{\Delta t^2}{\Delta z^2}\left(\frac{\lambda_2+2\mu_2}{\rho_2}\right)$$

$$c_4 = \frac{\Delta t^2}{\Delta r \Delta z}\left(\frac{\lambda_2+\mu_2}{2\rho_2}\right)$$

A2. Second Order Boundary Conditions for a Rigid Tool-Liquid Cylindrical Interface

The formulation for this case, which is analogous to the formulation for the liquid-solid interface presented in Appendix A1 is given below.

The wave equation in the homogeneous rigid tool to the left of the interface (see Figure 1) is:

$$\rho_0 u_{tt}^0 - (\lambda_0+2\mu_0)(u_{rr}^0 + \frac{1}{r}u_r^0 - \frac{1}{r^2}u^0) - \mu_0 u_{zz}^0 - (\lambda_0+\mu_0)w_{rz}^0 = 0 \qquad \text{(A2-1)}$$

$$\rho_0 w_{tt}^0 - \mu_0(w_{rr}^0 + \frac{1}{r}w_r^0) - (\lambda_0+2\mu_0)w_{zz}^0 - (\lambda_0+\mu_0)(u_{rz}^0 + \frac{1}{r}u_z^0) = 0 \qquad \text{(A2-2)}$$

and in the homogeneous liquid to the right of the interface is:

$$\rho_1 u_{tt}^1 - \lambda_1(u_{rr}^1 + \frac{1}{r}u_r^1 - \frac{1}{r^2}u^1) - \lambda_1 w_{rz}^1 = 0 \qquad \text{(A2-3)}$$

$$\rho_1 w_{tt}^1 - \lambda_1(u_{rz}^1 + \frac{1}{r}u_z^1) - \lambda_1 w_{zz}^1 = 0 \qquad \text{(A2-4)}$$

The boundary conditions which must hold at the rigid tool-liquid interface are a continuity of normal stress,

$$(\lambda_0+2\mu_0)u_r^0 + \lambda_0(\frac{1}{r}u^0 + w_z^0) = \lambda_1(u_r^1 + \frac{1}{r}u^1) + \lambda_1 w_z^1, \qquad \text{(A2-5)}$$

a vanishing of the tangential stress in the rigid tool,

$$\mu_0(u_z^0 + w_r^0) = 0, \qquad \text{(A2-6)}$$

a vanishing of the normal displacement,

$$u^0 = u^1 = 0. \qquad \text{(A2-7)}$$

a vanishing of the vertical displacement in the rigid tool,

$$w^0 = 0. \qquad \text{(A2-8)}$$

The superscripts 0 and 1 refer to values in the rigid tool and liquid respectively. The

only unknown in the derivation is the vertical displacement in the liquid at the interface, $w^1(T,n,l)$. The interface is at a radius of $R=T\Delta r$.

Additional relationships required in the derivation are the Taylor expansions:

$$\Delta r u_r^1+\frac{1}{2}\Delta r^2 u_{rr}^1=u^1(T+1,n,l)-u^1(T,n,l) \qquad \text{(A2-9)}$$

As in Appendix A1, by solving equations (A2-3), (A2-4), and (A2-9) for the vertical displacement in the liquid at the interface, one obtains:

$$\begin{aligned}
w^1(T,n,l+1)=&2w^1(T,n,l)-w^1(T,n,l-1)\\
&+b_1^*[w^1(T,n+1,l)-2w^1(T,n,l)+w^1(T,n-1,l)]\\
&+b_2^*[u^1(T,n+1,l)-u^1(T,n-1,l)]\\
&+b_3^*[u^1(T+1,n+1,l)-u^1(T,n+1,l)-u^1(T+1,n-1,l)+u^1(T,n-1,l)]\\
&+b_4^*[u^1(T,n+1,l+1)-2u^1(T,n+1,l)+u^1(T,n+1,l-1)\\
&\quad -u^1(T,n-1,l+1)+2u^1(T,n-1,l)-u^1(T,n-1,l-1)]\\
&+b_5^*[w^1(T+1,n+1,l)-2w^1(T+1,n,l)+w^1(T+1,n-1,l)\\
&\quad -w^1(T,n+1,l)+2w^1(T,n,l)-w^1(T,n-1,l)]\\
&+b_6^*[u^1(T+1,n+1,l)-u^1(T+1,n-1,l)-u^1(T,n+1,l)+u^1(T,n-1,l)]
\end{aligned}$$

where

$$b_1^*=\left[\frac{\Delta t^2}{\Delta z^2}\right]^2\frac{\lambda_1}{\rho_1}$$

$$b_2^*=\frac{\Delta t^2}{\Delta r\Delta z}\frac{\lambda_1}{2\rho_1}\left(\frac{1}{T}-\frac{1}{2T^2}\right)$$

$$b_3^*=\frac{\Delta t^2}{\Delta r\Delta z}\frac{\lambda_1}{2\rho_1}$$

$$b_4^*=-\frac{\Delta r}{4\Delta z}$$

$$b_5^*=\frac{\Delta t^2}{\Delta z^2}\frac{\lambda_1}{2\rho_1}$$

$$b_\theta^* = \frac{\Delta t^2}{\Delta z \Delta r} \frac{\lambda_1}{\rho_1} \frac{1}{4T.}$$

It is important to notice the similitude of the b^* coefficients of the rigid tool-liquid interface and the b coefficients of the liquid-solid interface, and also the complete equation for the vertical displacement in the fluid.

A3. The Source

Two different sources are used in the solution to the wave equation in the borehole case.

a) Point source in the borehole axis (absence of the rigid tool).

The source is a compressional point source in the fluid-filled borehole. The solution to the wave equation for the compressional displacement potential in a homogeneous liquid in cylindrical coordinate (r,z) is:

$$\varphi(r,z,t)=\frac{A}{4\pi\rho\alpha^2 R}g(t-R/\alpha) \tag{A3-1}$$

where $R = (r^2+z^2)^{1/2}$ is the distance between the source and the observation point,

α is the compressional wave velocity in the fluid,

ρ is the density of the fluid,

and A is a unit constant with dimensions of $(mass \times space \times length^2/\ time)$.

In our work the source time function is taken to be (Kelly *et al*, 1976)

$$g(t) = -2\xi T e^{-\xi T^2}, \qquad T = t - t_s \tag{A3-2}$$

where ξ is a pulse width parameter and t_s is a time shift parameter.

Since the displacement $\vec{u}$ is the gradient of the potential:

$$\vec{u}(r,z,t) = \begin{bmatrix} \frac{r}{R} \\ \frac{z}{R} \end{bmatrix} \frac{(-A)}{4\pi\rho\alpha^2}\left[\frac{g(t-R/\alpha)}{R^2} + \frac{g'(t-R/\alpha)}{R\alpha}\right] \tag{A3-3}$$

where

$$g'(t) = -2\xi(1-2\xi T^2)e^{-\xi T^2} \tag{A3-4}$$

Similarly, the solution to the pressure field $(p = \alpha^2\rho\nabla\cdot\vec{u} = \alpha^2\rho\nabla^2\varphi = -\rho\frac{\partial^2\varphi}{\partial t^2})$ is:

$$p(r,x,t) = \frac{-A}{4\pi\alpha^2 R} g''(t - R/\alpha) \qquad \textbf{(A3-5)}$$

where

$$g''(t) = 4\xi^2(3T - 2\xi T^2)e^{-\xi T^2} \qquad \text{(A3-6)}$$

and the Fourier Transform is :

$$F[g''(t)] = i\pi^{1/2}\xi^{-1/2}\omega^3 e^{-\omega^2/4\xi} e^{i\omega(t_s + R/\alpha)} \qquad \text{(A3-7)}$$

The peak frequency and bandwidth are determined from the pulse width parameter, ξ. For a pressure source, from equation (A3-7), the peak frequency is given by

$$f_{peak} = 0.39\sqrt{\xi} \qquad \text{(A3-8)}$$

with the upper-half-power and the lower-half-power frequencies given by $0.528\xi^{1/2}$ and $0.266\xi^{1/2}$, respectively. The bandwidth, defined by the distance between the two half-power points, is given by $0.262\xi^{1/2}$. In terms of f_{peak} the values of t_s and t_{max} are set to:

$$t_s = -\frac{R_{min}}{\alpha} + \frac{1.46}{f_{peak}} \qquad \text{(A3-9)}$$

$$t_{max} = t_s + \frac{R_{max}}{\alpha} + \frac{1.46}{f_{peak}} \qquad \text{(A3-10)}$$

b) Source in the surface of a rigid tool.

In this case a source model was prepared by White and Zechman [1968], Bhasavanija [1983] and consists of the product of two functions. The radial displacement at the rigid tool wall is defined by:

$$u_r = f(t).g(z) \qquad \text{(A3-11)}$$

where $f(t)$ is a Ricker wavelet [Ricker, 1977] in the time domain and $g(z)$ the source strength distribution along the tool wall.

The Ricker wavelet is defined as:

$$f(t)=(1-\frac{2(t-t_0)^2}{a^2})\exp(-\frac{(t-t_0)^2}{a^2}) \qquad \text{(A3-12)}$$

if $0 < t < 2t_0$ and, $f(t)= 0$ for $t > 2t_0$, where t_0 is the time when the maximum peak occurs, and $a^2=\frac{4}{\omega^2_0}$ uses the value of ω_0, the peak frequency of the source spectrum.

In the case of the $g(z)$ distribution, the following definition is used:

$$g(z)=\frac{1}{2\pi^2 C}\left\{Si\left[C(z-z_0)+\pi\right]-Si\left[c(z-z_0)-\pi\right]\right\} \qquad \text{(A3-13)}$$

where z_0 is the center of the source and C is 2π divided by the source length. The function Si is defined in Abramowitz and Stegun [1964].

REFERENCES

Abramowitz M. and Stegun I., 1964. Handbook of Mathematical Functions. Dover Publications.

Aki, K. and Richards, P.G. 1980. Quantitative Seismology: Theory and Methods, W.W. Freeman and Company, San Francisco.

Alterman , Z., and Karal F.C., 1968. Propagation of elastic waves in layered media by finite difference methods. Bull. Seism. Soc. Am. *58*, 367-398.

Alterman, Z., and Loewenthal, D. 1972. Computer generated seismograms. In: Methods in Computational Physics, v. 12: Bolt, B.A., Ed., Academic Press, New York, 35-164.

Baker L.J., 1984. The effect of the invaded zone on full wave train acoustic logging. Geophysics, *49*, 796-809.

Bamberger, A., Chavent, G. and Lailly, P. 1980. Etudes de schemas numeriques pour les equations de l'elastodynamique lineaire. Rapports de Recherche, *41*, INRIA, B.P. 105, 78150 Le Chesnay, France.

Biot, M.A. 1952. Propagation of elastic waves in a cylindrical bore containing a fluid. J. Appl. Phys., *23*, 997-1005.

Bhasavanija K. 1983. A Finite Difference Model of an Acoustic Logging Tool: the Borehole in a Horizontally Layered Geologic Medium. Ph D thesis. Colorado School of Mines. Golden, Colorado.

Boore, D.M. 1972. Finite difference methods for seismic waves. In: Methods in computational Physics, v. 11: Bolt, B.A., Ed., Academic Press, New York, 1-37.

Bouchon M. and Aki K. 1977. Discrete wavenumber representation of seismic source wave fields. Bull. Seism. Soc. Am., *67*, 259-277.

Chang S.K. and Everhart A.H., 1983. A study of sonic logging in a cased borehole. J. Pet. Tech. *35*, 1745-1750.

Cheng, C.H. and Toksöz, M.N. 1981. Elastic wave propagation in a fluid-filled borehole and synthetic acoustic logs. Geophysics, *46*, 1042-1053.

Chin R.C.Y., Hedstrom G and Thigpen L. 1982. Numerical methods in seismology. submitted for publication to Journal of Computational Physics.

Clayton, R. and Engquist, B. 1977. Absorbing boundary conditions for acoustic and elastic wave equations. Bull. Seism. Soc. Am., *67*, 1529-1540.

Emerman, S.H. and Stephen, R.A. 1983. Comment on, "Absorbing boundary conditions for acoustic and elastic wave equations," by R. Clayton and B. Engquist. Bull. Seism. Soc. Am. *73*, 661-665.

Fuyuki, M. and Y. Matsumoto 1980. Finite difference analysis of Rayleigh wave scattering at a trench, Bull. Seism. Soc. Am., *67*, 1529-1540.

Jacobi W.L. 1949. Propagation of sound waves along liquid cylinders, J. Acoust. Soc. Am., *21*, 120-127.

Johnston D.H. 1978. The attenuation of seismic waves in dry and saturated rocks, Ph. D. thesis Mass. Inst. of Technol., Cambridge.

Kelly, K.R., Ward, R.W., Treitel, S., and Alford, R.M. 1976. Synthetic seismograms: A finite difference approach. Geophysics, *41*, 2-27.

Ottaviani M., 1971. Elastic wave propagation in two evenly-welded quarter-spaces, Bull Seism., Soc. Am., *61*, 1119-1152.

Paillet F., 1980. Acoustic propagation in the vicinity of fractures which intersect a fluid-filled borehole. Trans. of 21st Ann. Logging Symp. of SPWLA, July 8-11.

Paillet F. and White J.E., 1982. Acoustic modes of propagation in the borehole and their relationship to rock properties, Geophysics, *47*, 1215-1228.

Peterson E.W., 1974. Acoustic wave propagation along a fluid-filled cylinder. J. of Applied Physics, *45*, 3340-3350.

Reynolds A.C., 1978. Boundary conditions for the numerical solution of wave propagation problems. Geophysics, *43*, 1099-1110.

Ricker N.H., 1977. Transient waves in visco-elastic media: Elsevier Scientific Publishing Co., New York.

Rosenbaum, J.H., 1974. Synthetic microseismograms: logging in porous formations. Geophysics, *39*, 14-32.

Sato Y. and Ishihara K. 1983. On the numerical calculation of wave propagation by the finite difference method. Bull. Earthq. Res. Inst., *58*, 163-173.

Schoenberg M., Marzetta T., Aron J. and Porter R., 1982. Space-time dependence of acoustic waves in a borehole. J. Acoust. Soc. Am. *70*, 1496-1507.

Somers, E.V., 1953. Propagation of acoustic waves in a liquid filled cylindrical hole, surrounded by an elastic solid. J. Appl. Phys. *24*, 515-521.

Stephen, R.A. 1983. A comparison of finite difference and reflectivity seismograms for marine models. Geophys. J.R. Astr. Soc., *72*, 39-57.

Trefethen L. 1982. Wave Propagation and Stability for Finite Difference Schemes. Ph. D. Thesis. Stanford University. Stanford, California.

Tsang, L. and D. Rader 1979. Numerical evaluation of the transient acoustic waveform due to a point source in a fluid-filled borehole. Geophysics, *44*, 1706-1720.

Tubman K.M., Cheng C.H. and Toksöz M.N., 1984. Synthetic full waveform acoustic logs in cased boreholes. Geophysics, *49*, 1051-1059.

White, J.E. 1962. Elastic waves along a cylindrical bore. Geophysics, *27*, 327-333.

White, J.E. 1967. The hula log: a proposed acoustic log. Presented at the Eighth Ann.

Symp. of the SPWLA, Paper I

White, J.E. and R.E. Zechman 1968. Computed response of an acoustic logging tool. Geophysics, *33*, 302-310.

Wyatt S.B., 1979. The propagation of elastic waves along a fluid-filled annular region. Masters thesis, University of Tulsa, OK.

FIGURE CAPTIONS

Figure 1. Outline of the geometry used for finite difference synthetic acoustic logs in open hole case. Co-ordinates and types of boundaries are shown.

Figure 2. Outline of the geometry used for finite difference synthetic acoustic logs with rigid tool. Co-ordinates and types of boundaries are shown.

Figure 3. Synthetic acoustic log by Cheng and Toksöz [1981].

Figure 4. Dispersion curves for Stoneley and reflected conical waves modified from Cheng and Toksöz [1981].

Figure 5. Density and velocity model parameters used in the present paper. The tool radius is 4.5 cm.

Figure 6. (a) Discrete wavenumber (DW), and (b) finite difference (FD) synthetic seismogram at 2.2 m. The center frequency of the source is 15 kHz. (Model 1)

Figure 7. (a) Discrete wavenumber (DW), and (b) finite difference (FD) synthetic seismogram at 2.2 m. The center frequency of the source is 10.6 kHz. (Model 1)

Figure 8. (a) Frequency spectrum of the DW synthetic seismogram in Figure 4a. Notice the energy at about 23kHz. (b) Frequency spectrum of the DW synthetic seismogram in Figure 5a.

Figure 9. FD synthetic seismograms using Model 2 in an open hole. The center frequency is 12 Khz.

Figure 10. DWN synthetic seismograms using Model 2 in an open hole. The center frequency is 12 Khz.

Figure 11. FD synthetic seismograms using Model 2 and a rigid tool. The center frequency is 12 Khz.

Figure 12. DWN synthetic seismograms using Model 2 and a rigid tool. The center frequency is 12 Khz.

Figure 13. Velocity distribution used in the analysis of the depth of investigation.

Figure 14. Ray trace in a linear gradient zone. (change of gradient zone size)

Figure 15. Ray trace of a linear gradient zone. (change of formation velocity)

Figure 16. Table presenting the minimum source-receiver separation z necessary to "see" the formation.

Figure 17. FD synthetic seismograms using Model 3 in an open hole with a damaged zone. The center frequency is 12 Khz.

Figure 18. FD synthetic seismograms using Model 3 in a damaged zone with a rigid tool. The center frequency is 12 Khz.

Figure 19. FD synthetic seismogram travel time picks using Model 4, compared with the predicted travel time from ray theory.

Figure 20. FD record section using Model 2 in a damaged zone in an open hole.

Figure 21. FD record section using Model 2 in a damaged zone with a rigid tool.

Figure 22. Snapshots of the vertical displacement for the case in Figure 20.

Figure 23. Snapshots of the vertical displacement for the case in Figure 21.

Figure 24. Velocity distribution used in the analysis of the flushed zone.

Figure 25. FD record section using Model 6 in a (big) flushed zone with a rigid tool.

Figure 26. FD record section using Model 9 in a (big) damaged zone with a rigid tool.

Figure 27. FD record section using Model 5 in a (small) flushed zone with a rigid tool.

Figure 28. FD record section using Model 8 in a (big) flushed zone with a rigid tool.

Figure 29. FD record section using Model 7 in a (small) flushed zone with a rigid tool.

Figure 30. FD record section using Model 3 in a (small) damaged zone with a rigid tool.

Figure 31. FD record section using Model 8 in a (big) flushed zone with a rigid tool.

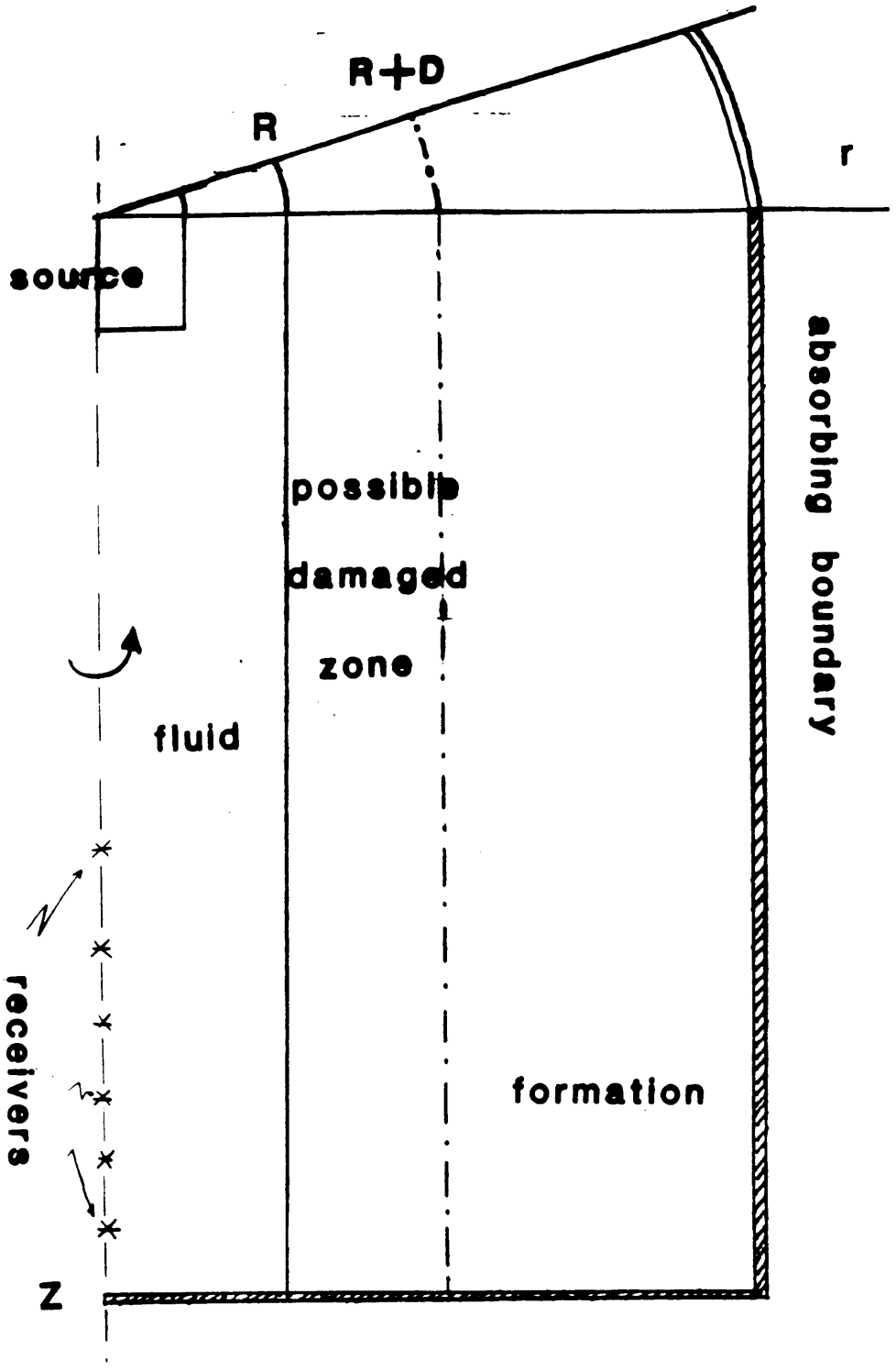
R+D
R
r
source
possible
damaged
zone
fluid
absorbing boundary
receivers
formation
Z

Figure 1

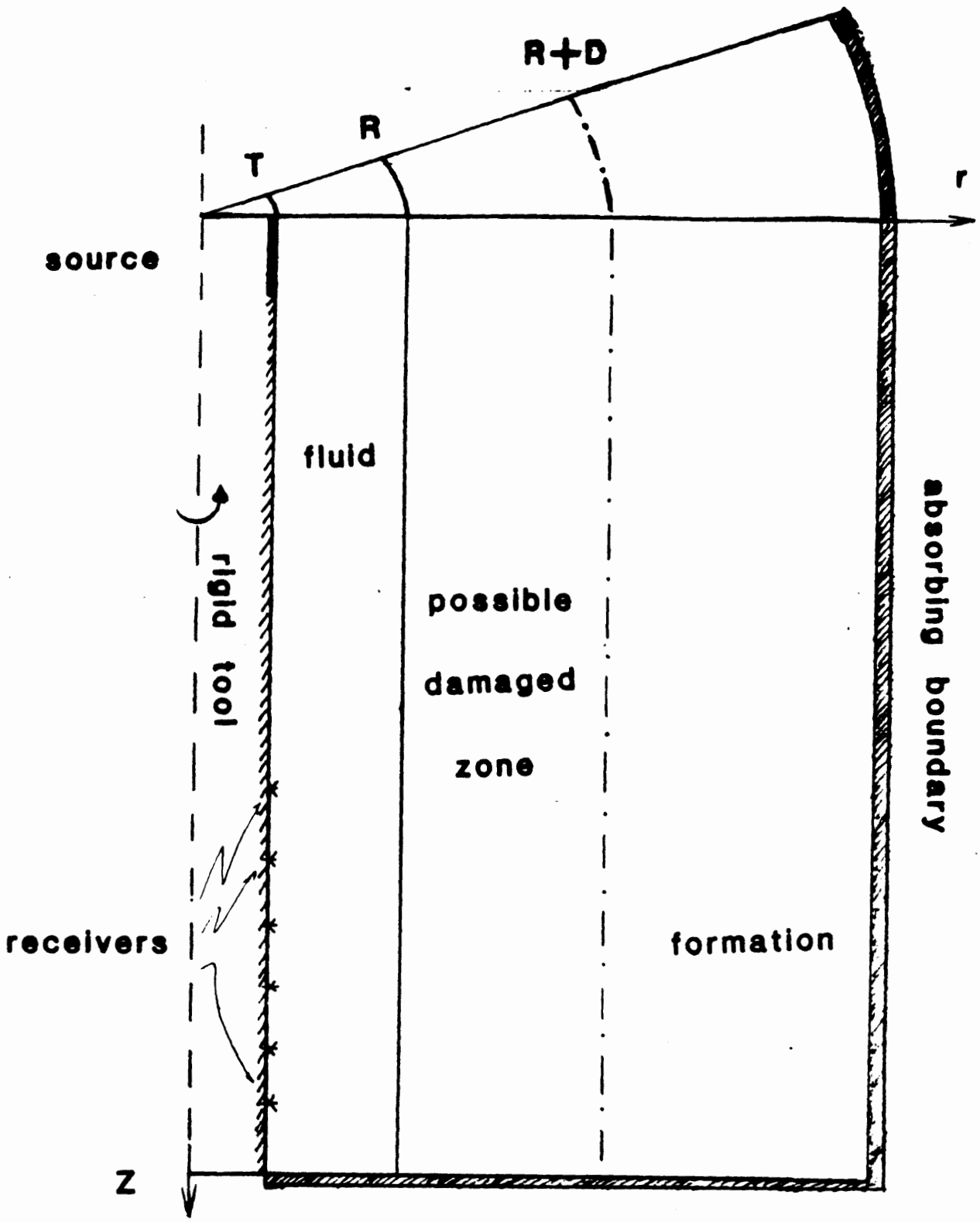
R+D
R
T
r
source
fluid
rigid tool
possible
damaged
zone
absorbing boundary
receivers
formation
Z

Figure 2

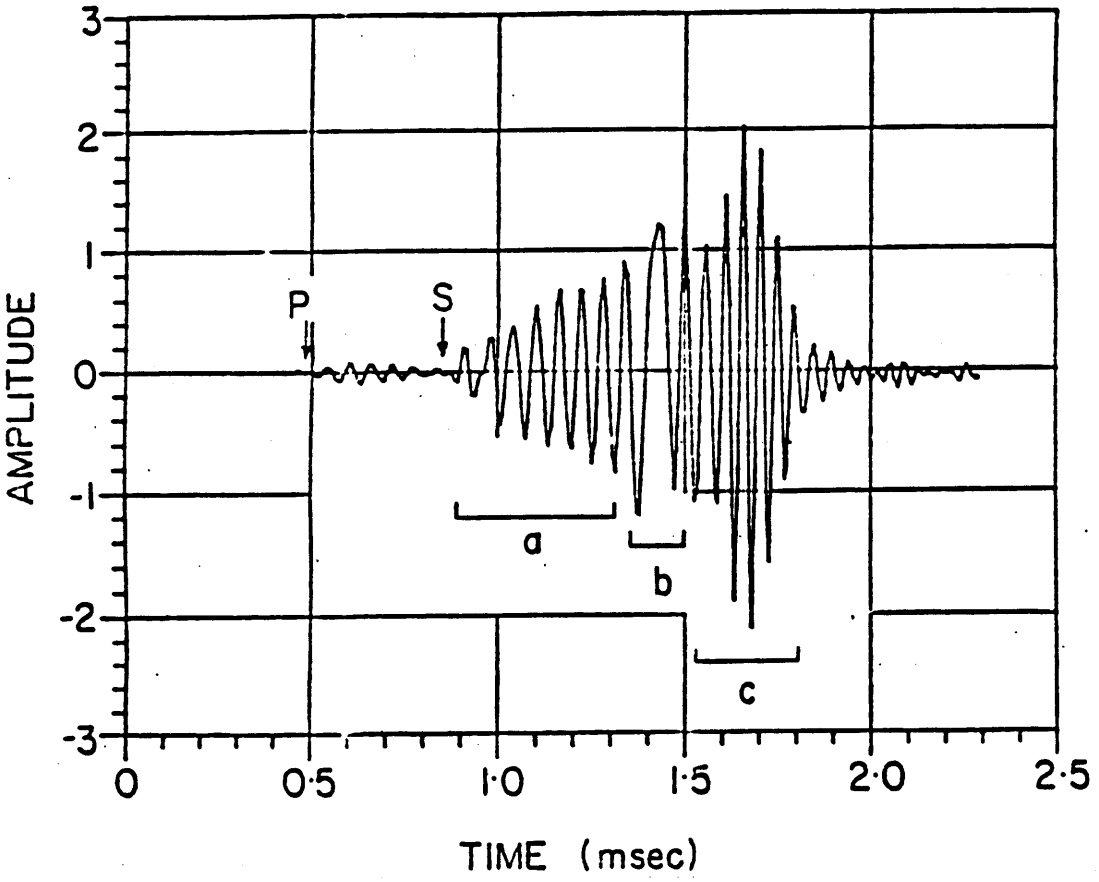

Figure 3

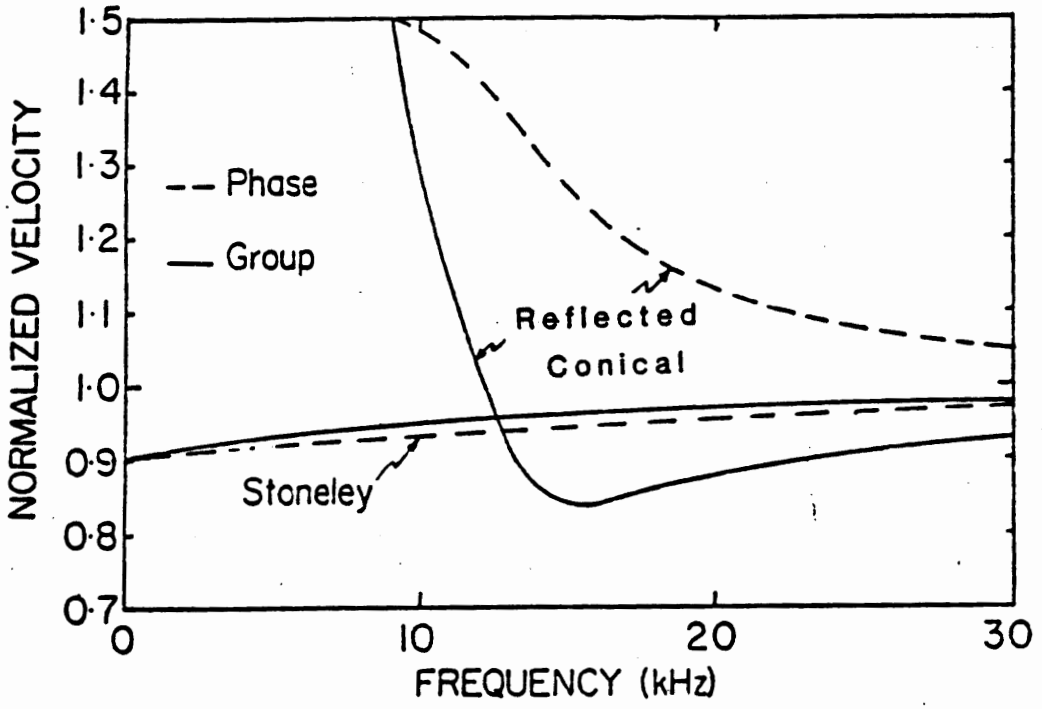
NORMALIZED VELOCITY
1·5
1·4
1·3
1·2
1·1
1·0
0·9
0·8
0·7
0
10
20
30
FREQUENCY (kHz)
Phase
Group
Reflected
Conical
Stoneley

Figure 4

MODEL PARAMETERS										
Model	v_f	ρ_f	R	v_{p0}	v_{s0}	ρ_0	D	v_{p1}	v_{s1}	ρ_1
1	1.80	1.20	10					4.00	2.30	2.30
2	1.65	1.50	9					4.00	2.30	2.30
3	1.65	1.50	9	3.63	2.18	2.37	9	4.00	2.30	2.30
4	1.80	1.50	10	3.00	1.72	2.30	10	4.00	2.30	2.30
5	1.65	1.50	9	4.13	2.27	2.37	9	4.00	2.30	2.30
6	1.65	1.50	9	4.13	2.27	2.37	27	4.00	2.30	2.30
7	1.65	1.50	9	4.00	2.30	2.37	9	3.50	2.30	2.30
8	1.65	1.50	9	4.00	2.30	2.37	27	3.50	2.30	2.30
9	1.65	1.50	9	3.63	2.18	2.37	27	4.00	2.30	2.30

v_f , v_{p0} , v_{s0} , v_{p1} , v_{s1} in Km/sec; ρ_f , ρ_0 , ρ_1 in gm/cc, R and D in cm.

Figure 5

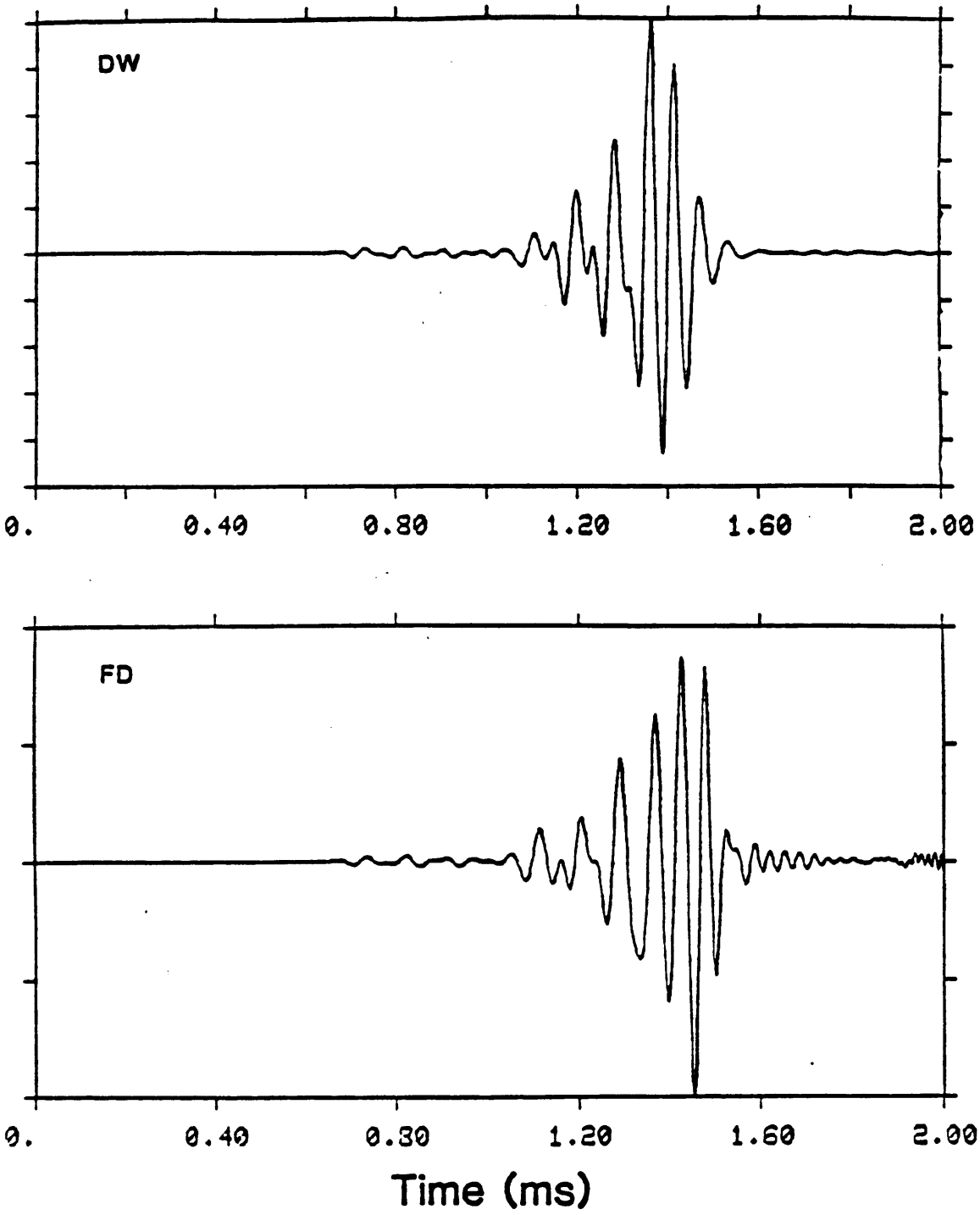

Figure 6

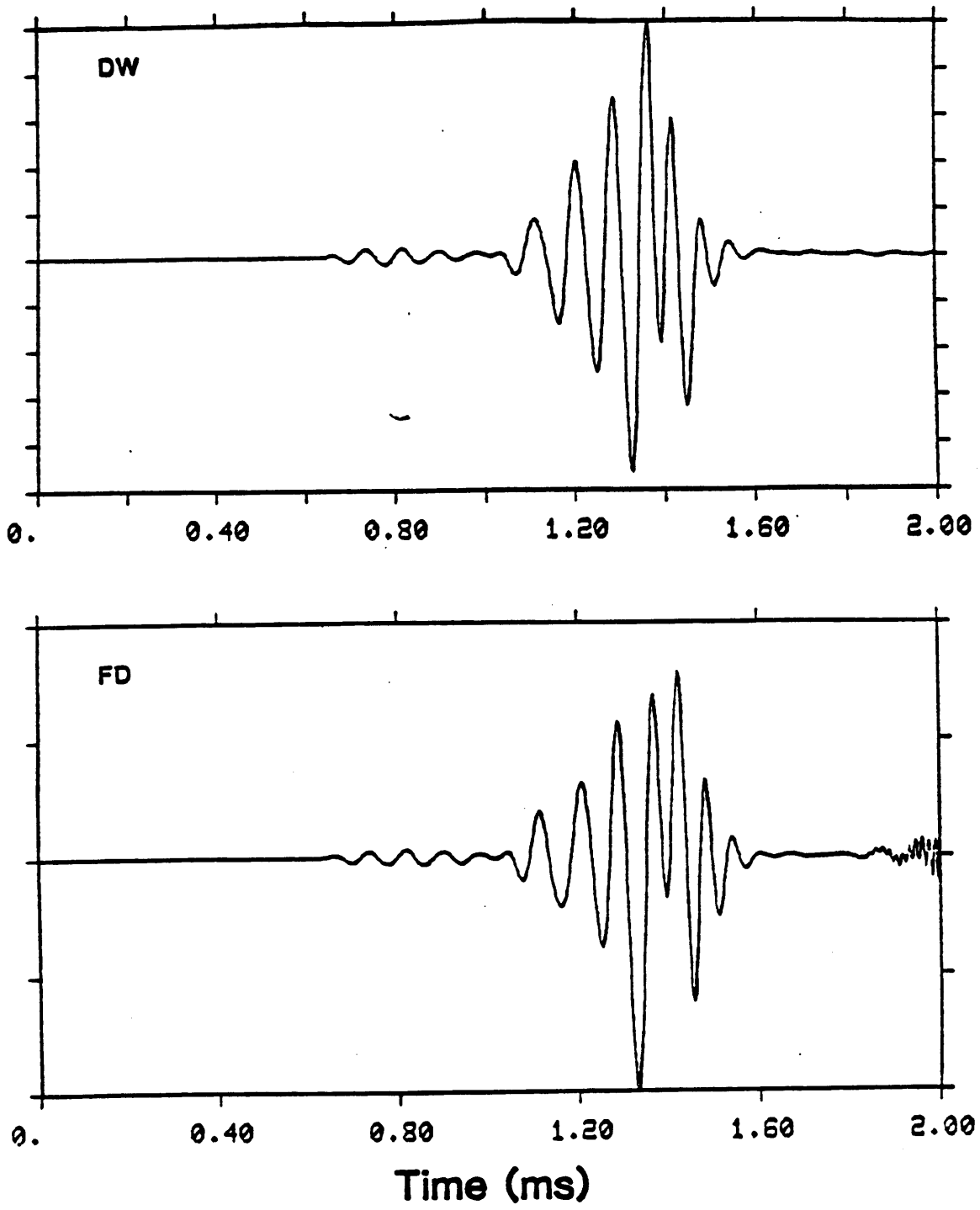

Figure 7

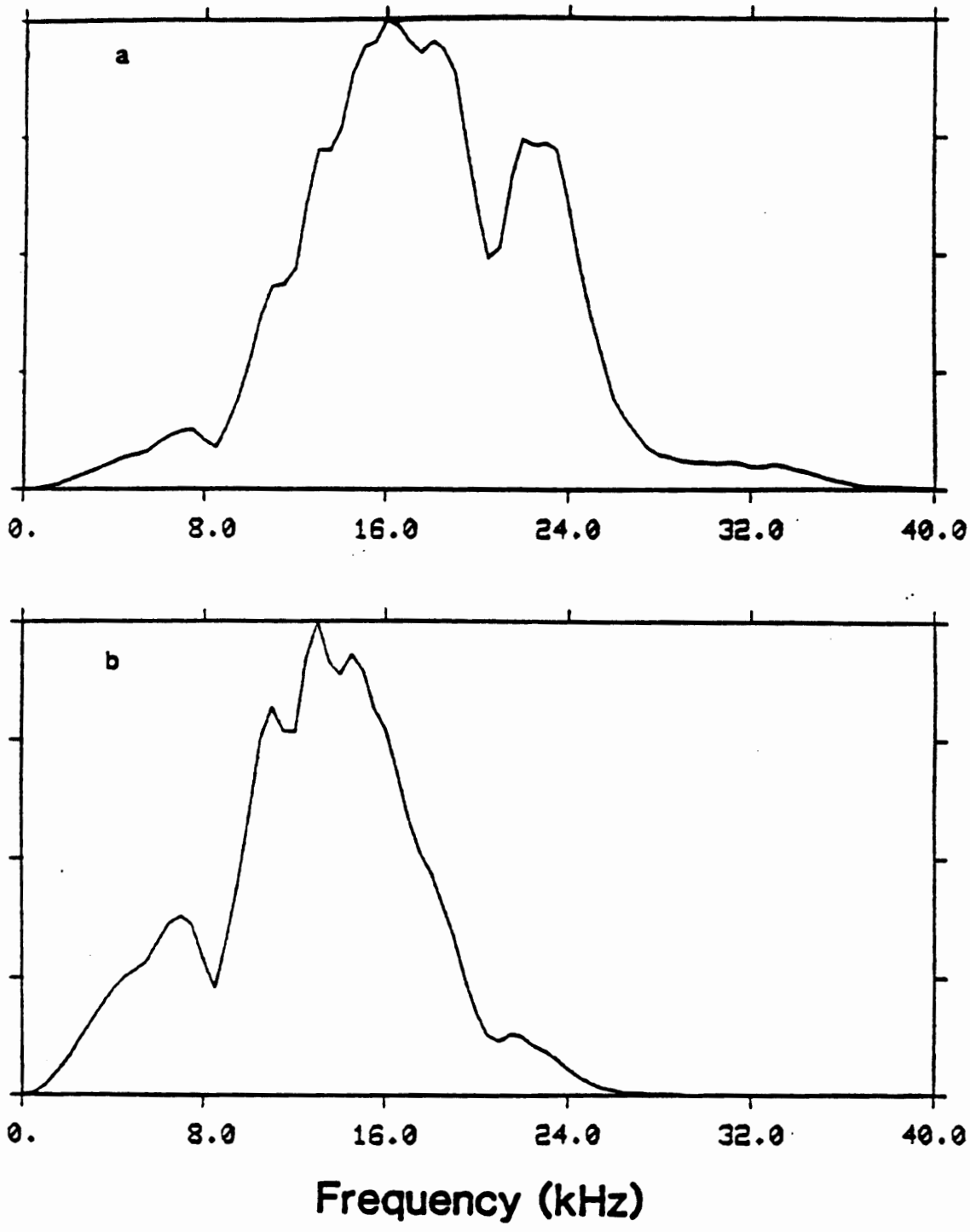

Figure 8

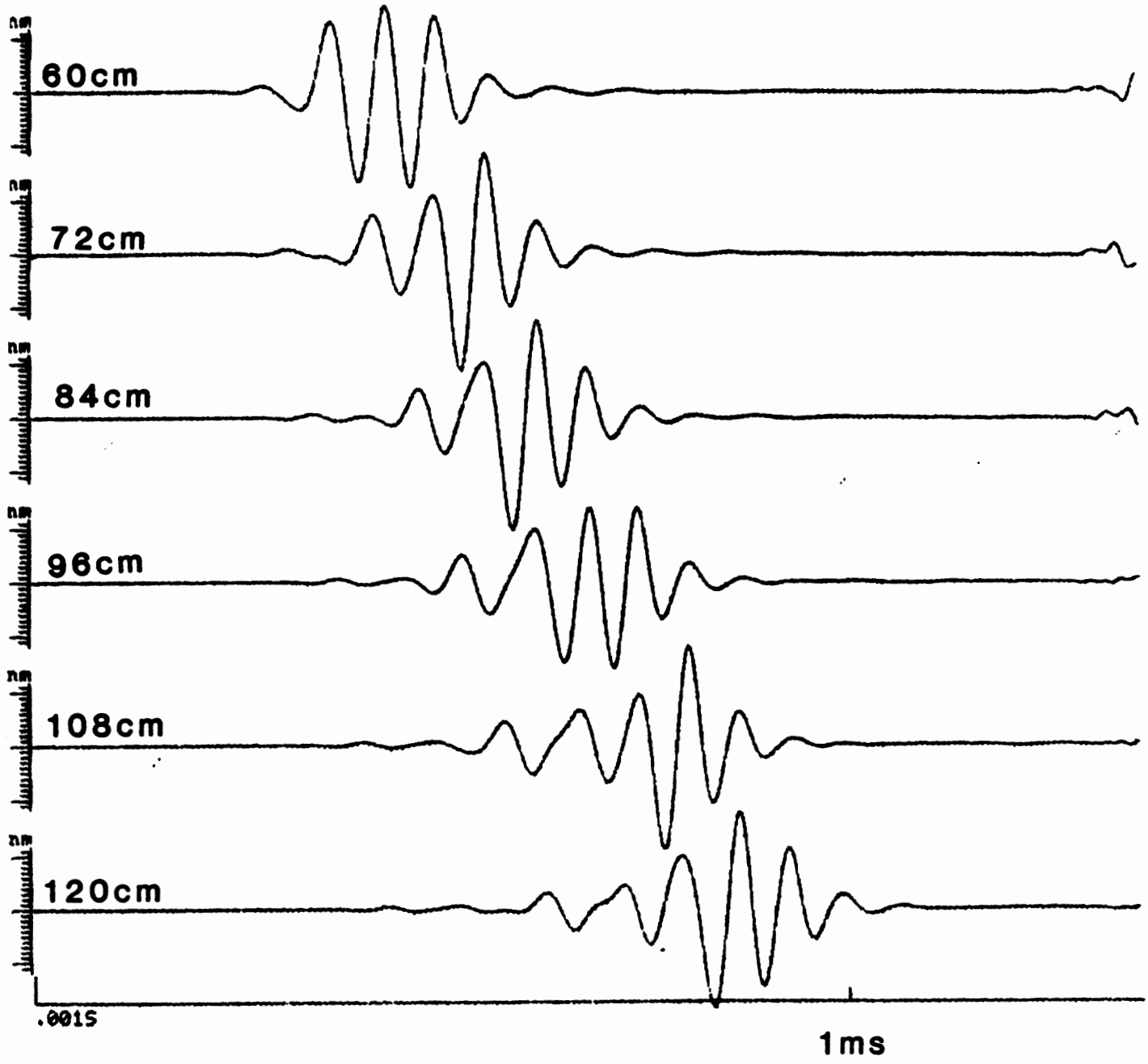

Figure 9

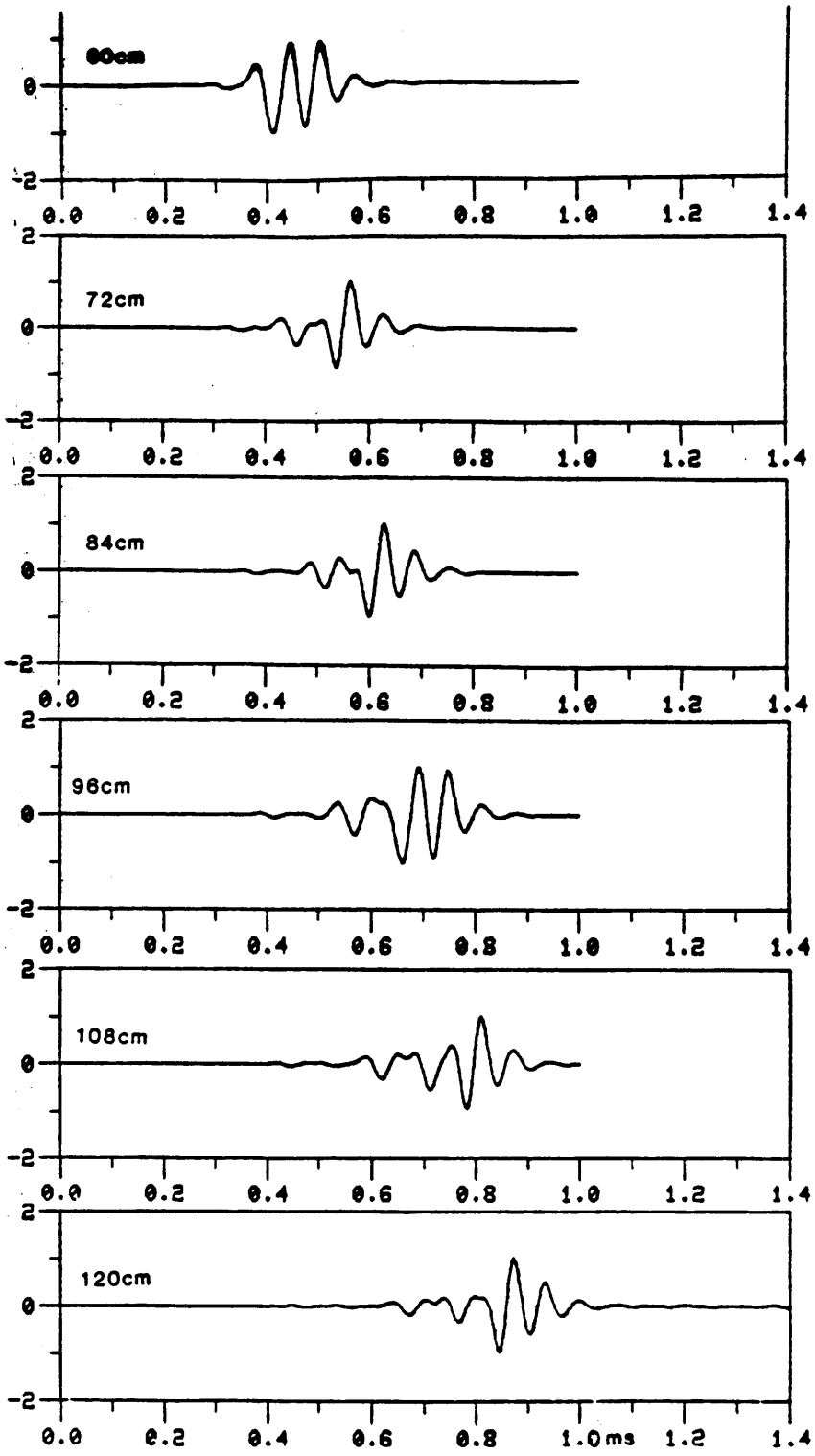

Figure 10

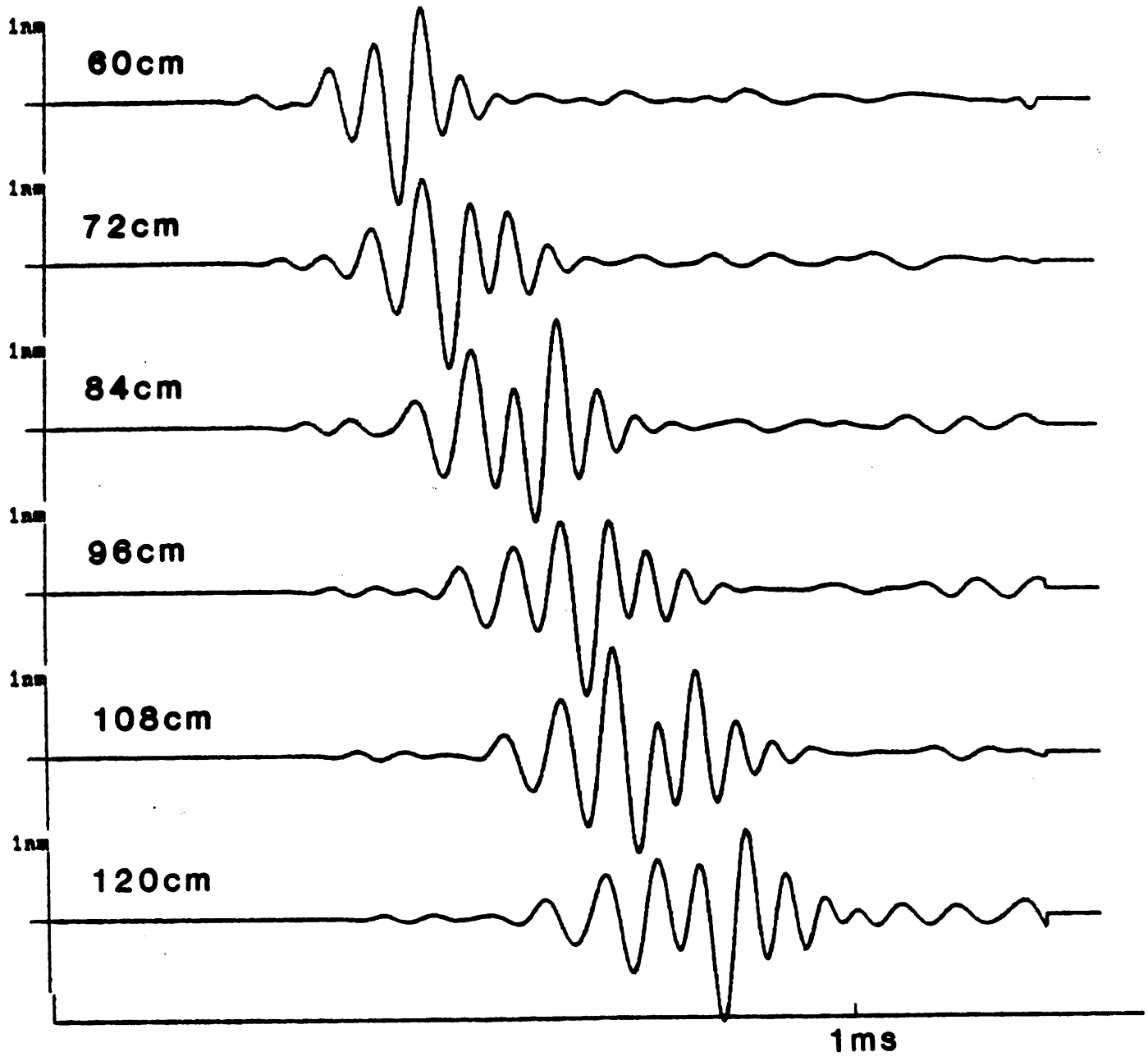

Figure 11

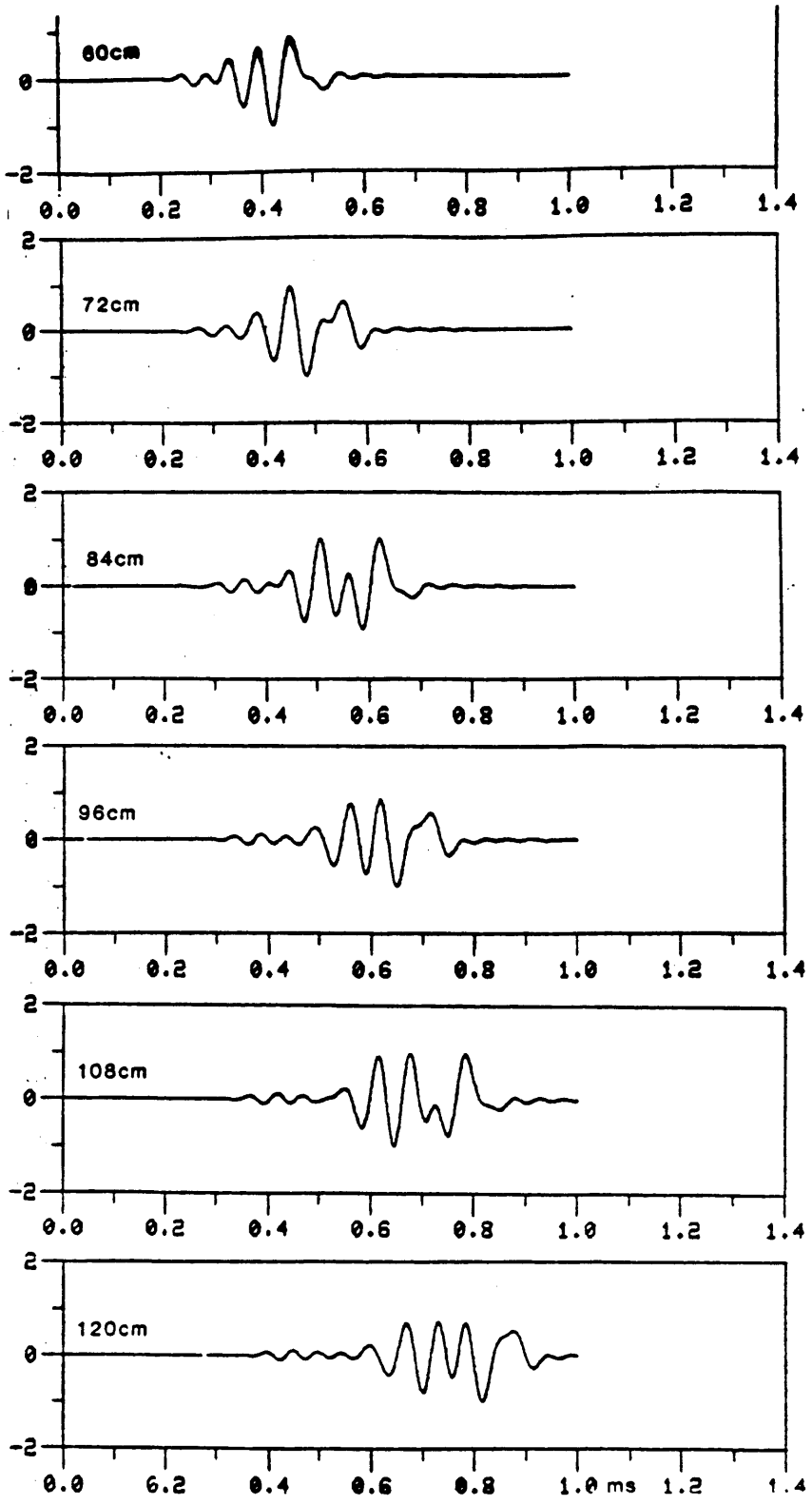

Figure 12

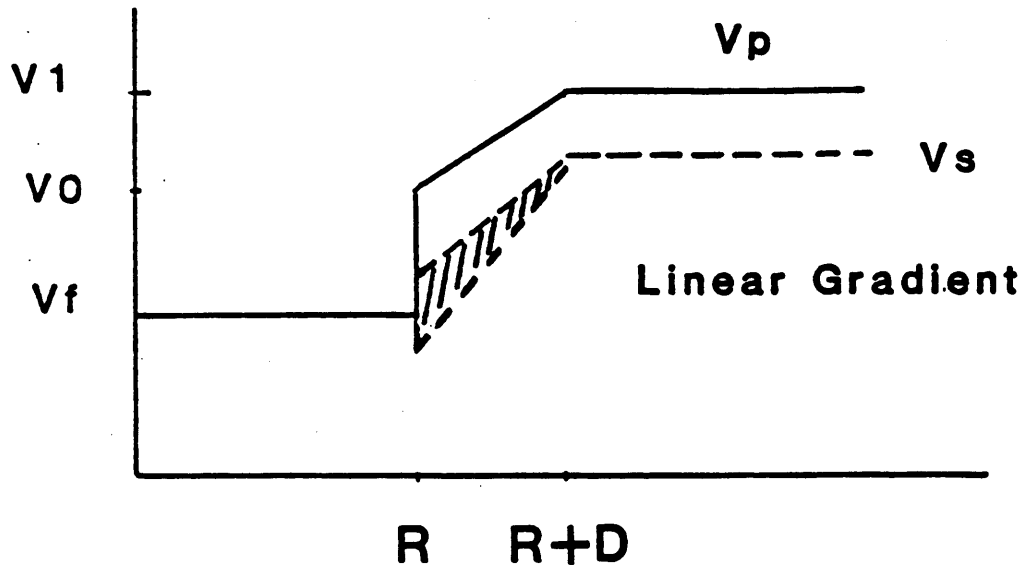

Figure 13

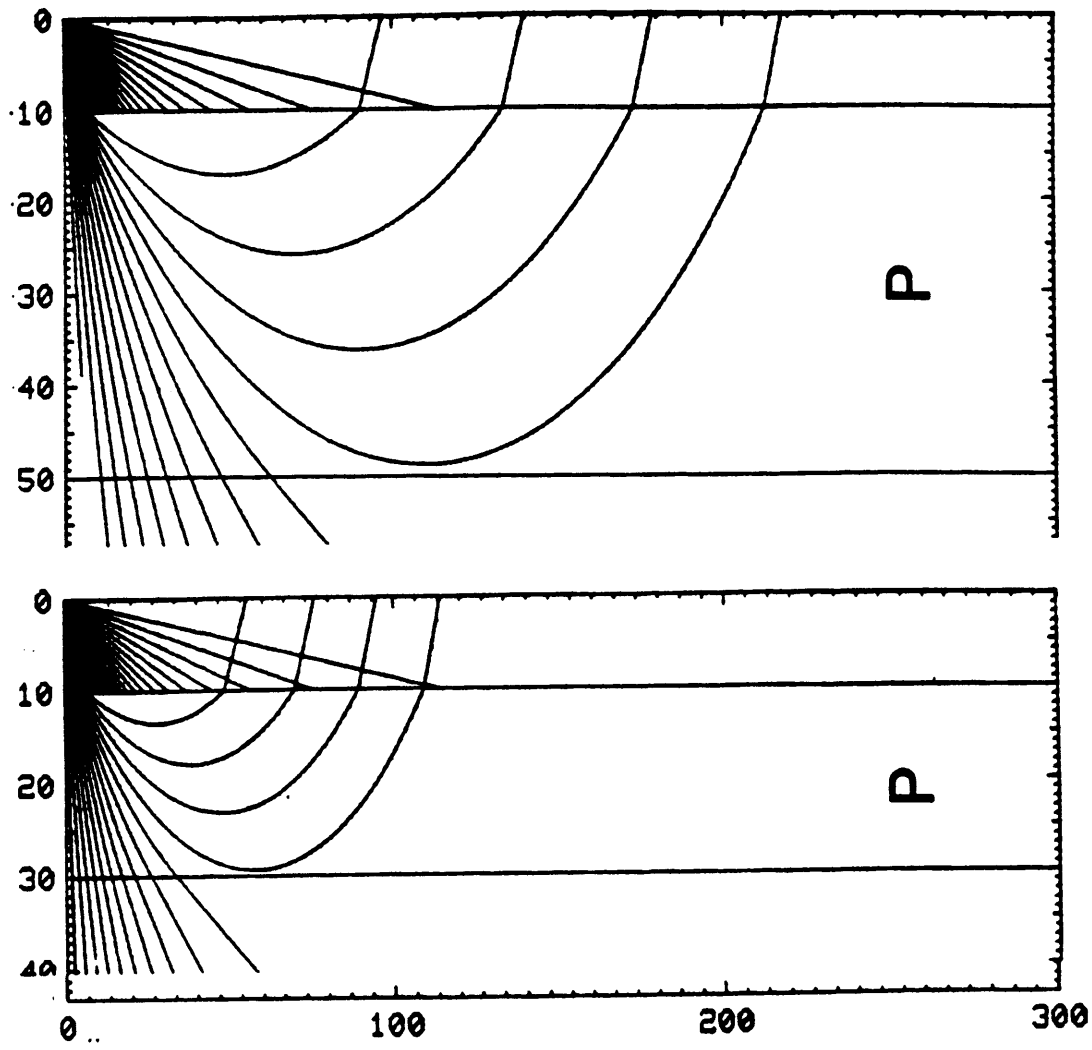

Vf: 1.8

V0: 3.0

V1: 4.0

Units in cm & Km/sec

Figure 14

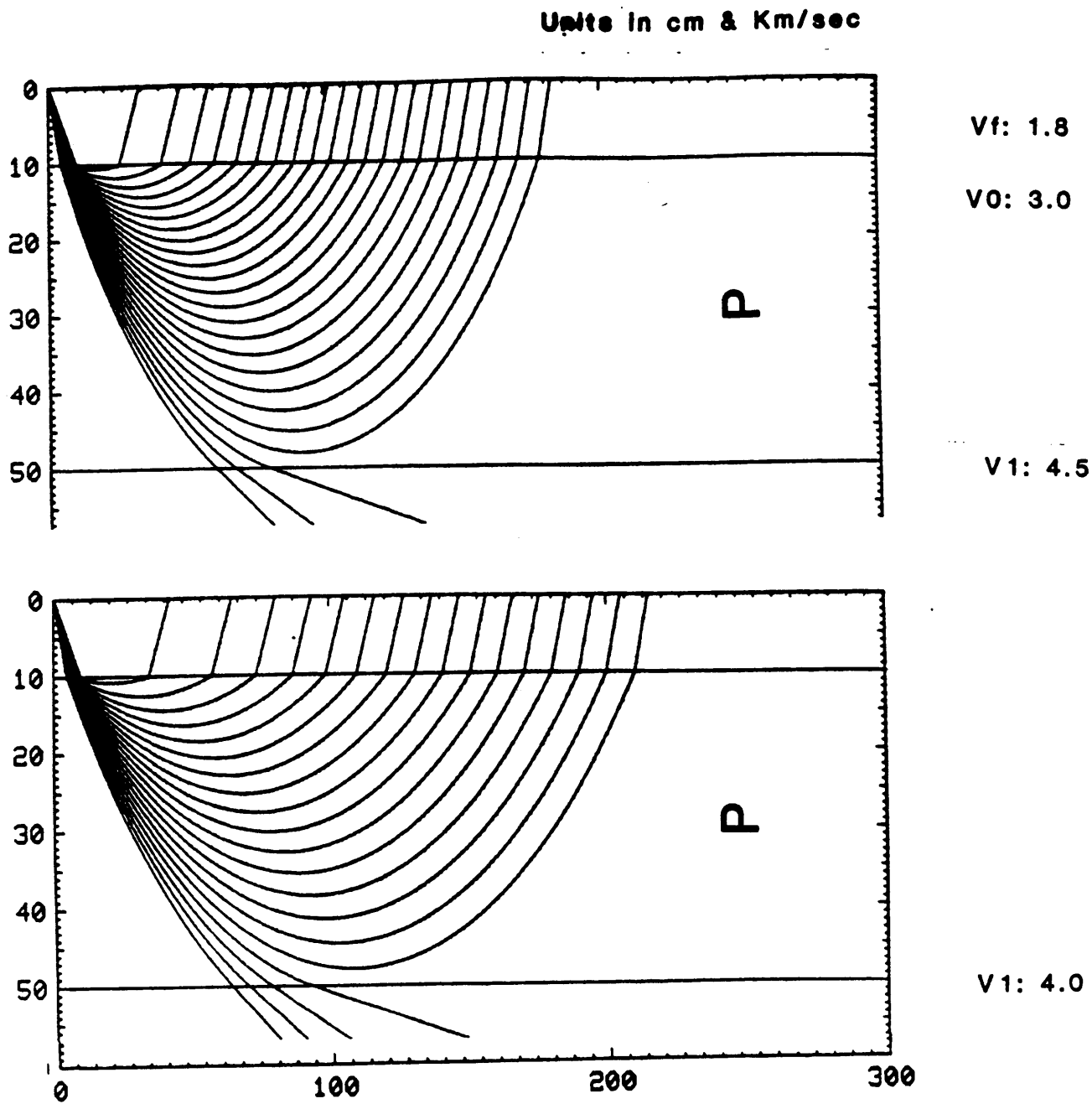
Units in cm & Km/sec
0
10
20
30
40
50
P
Vf: 1.8
V0: 3.0
V1: 4.5
0
10
20
30
40
50
P
V1: 4.0
0
100
200
300

Figure 15

v_f km/s	R m	v_0 km/s	D m	v_1 km/s	z m
1.8	0.1	3.0	0.1	4.0	0.63
1.8	0.1	3.5	0.1	4.0	0.88
1.8	0.1	2.5	0.2	4.0	0.93
1.8	0.1	3.0	0.2	4.0	1.16
1.8	0.1	3.5	0.2	4.0	1.65
1.8	0.1	2.5	0.3	4.0	1.35
1.8	0.1	3.0	0.3	4.0	1.69
1.8	0.1	3.5	0.3	4.0	2.43

Figure 16

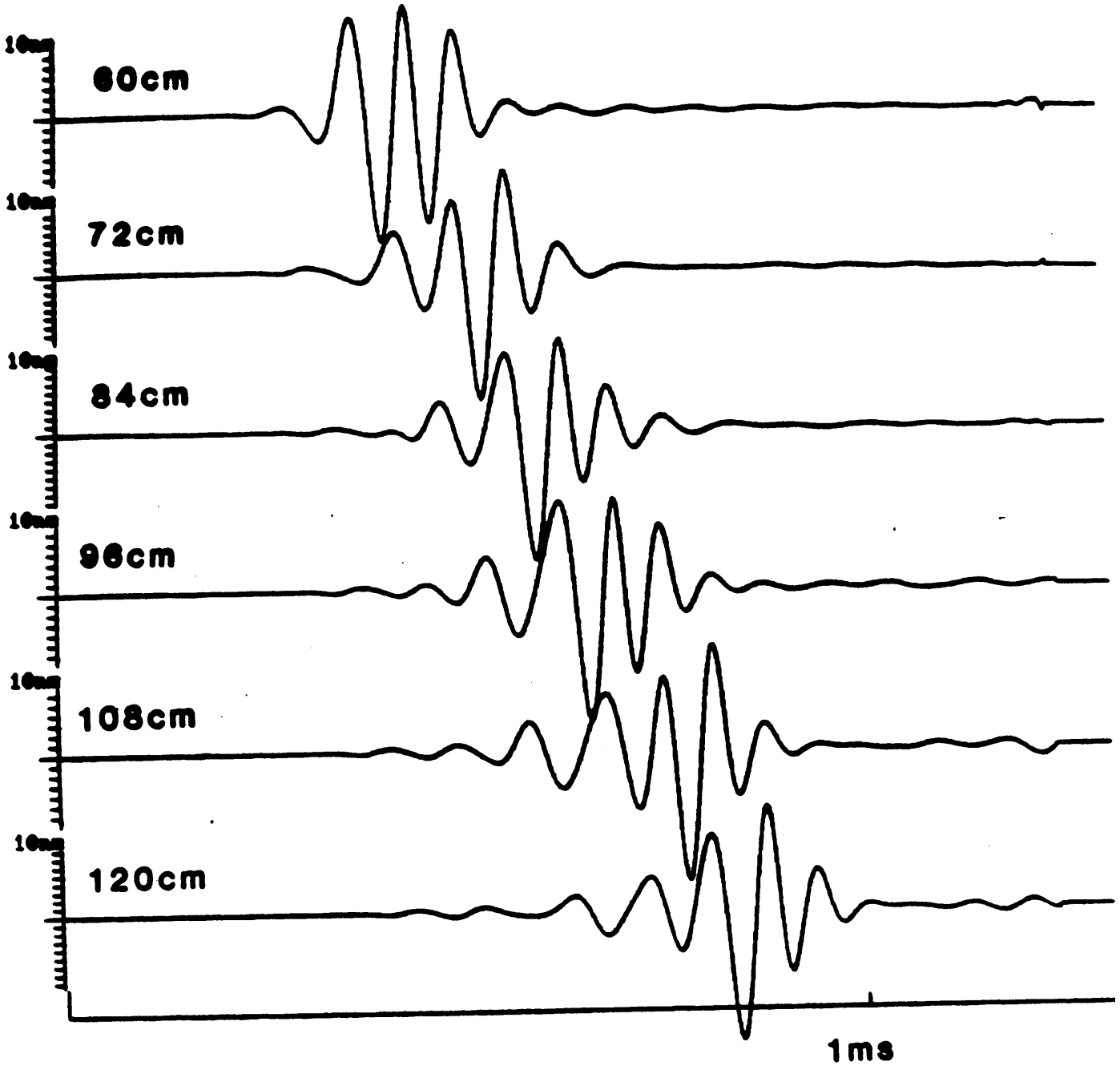

Figure 17

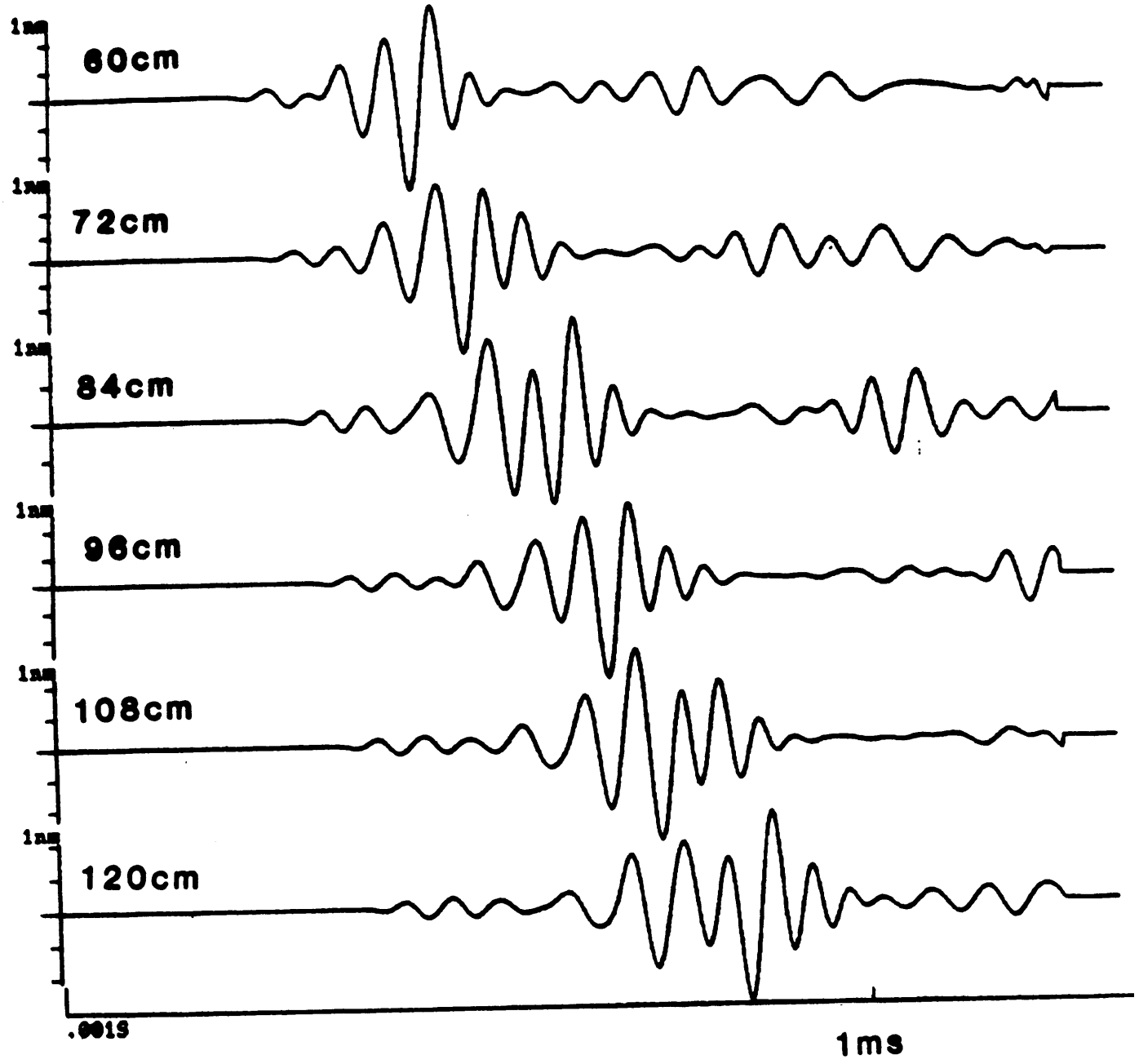

Figure 18

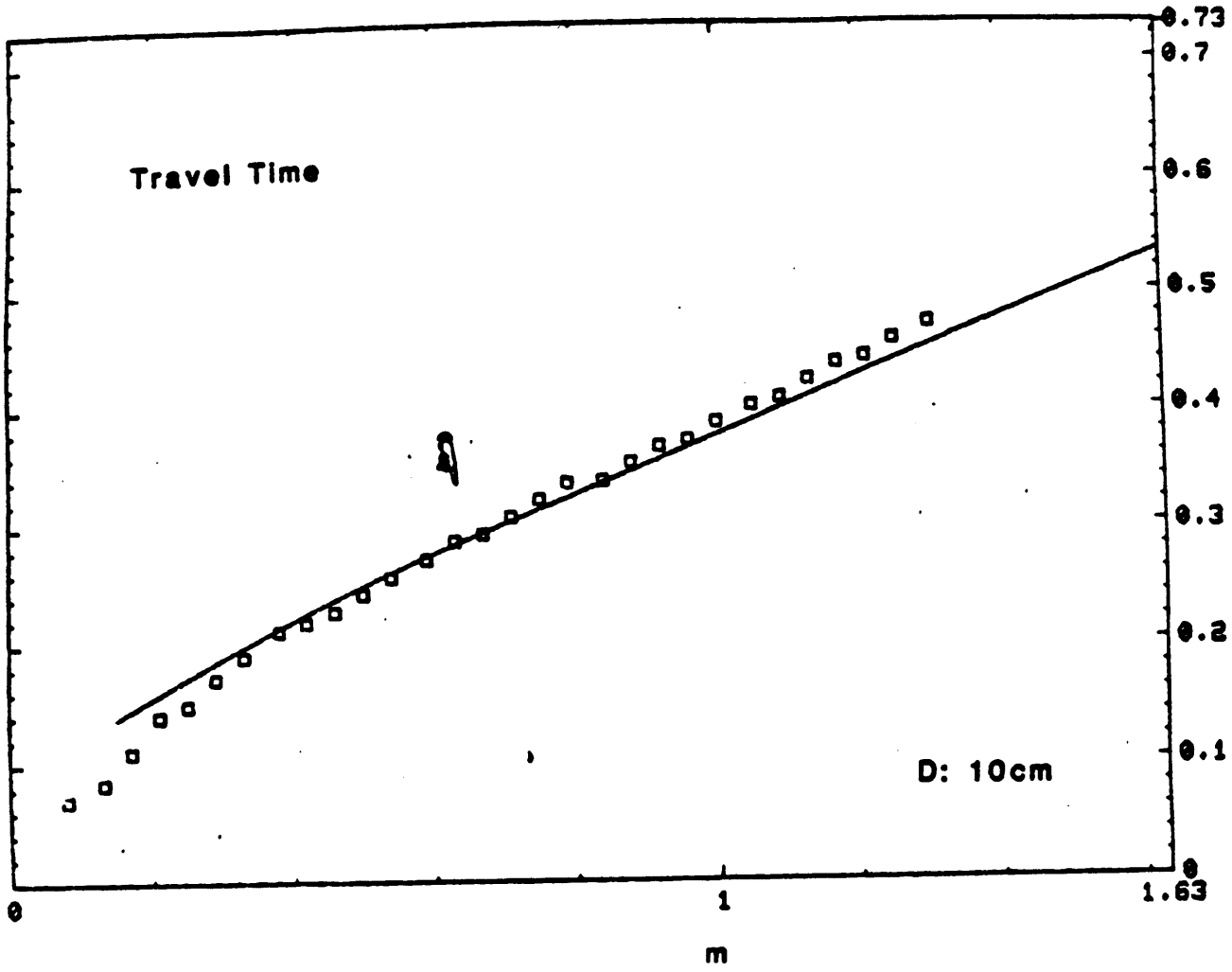

Figure 19

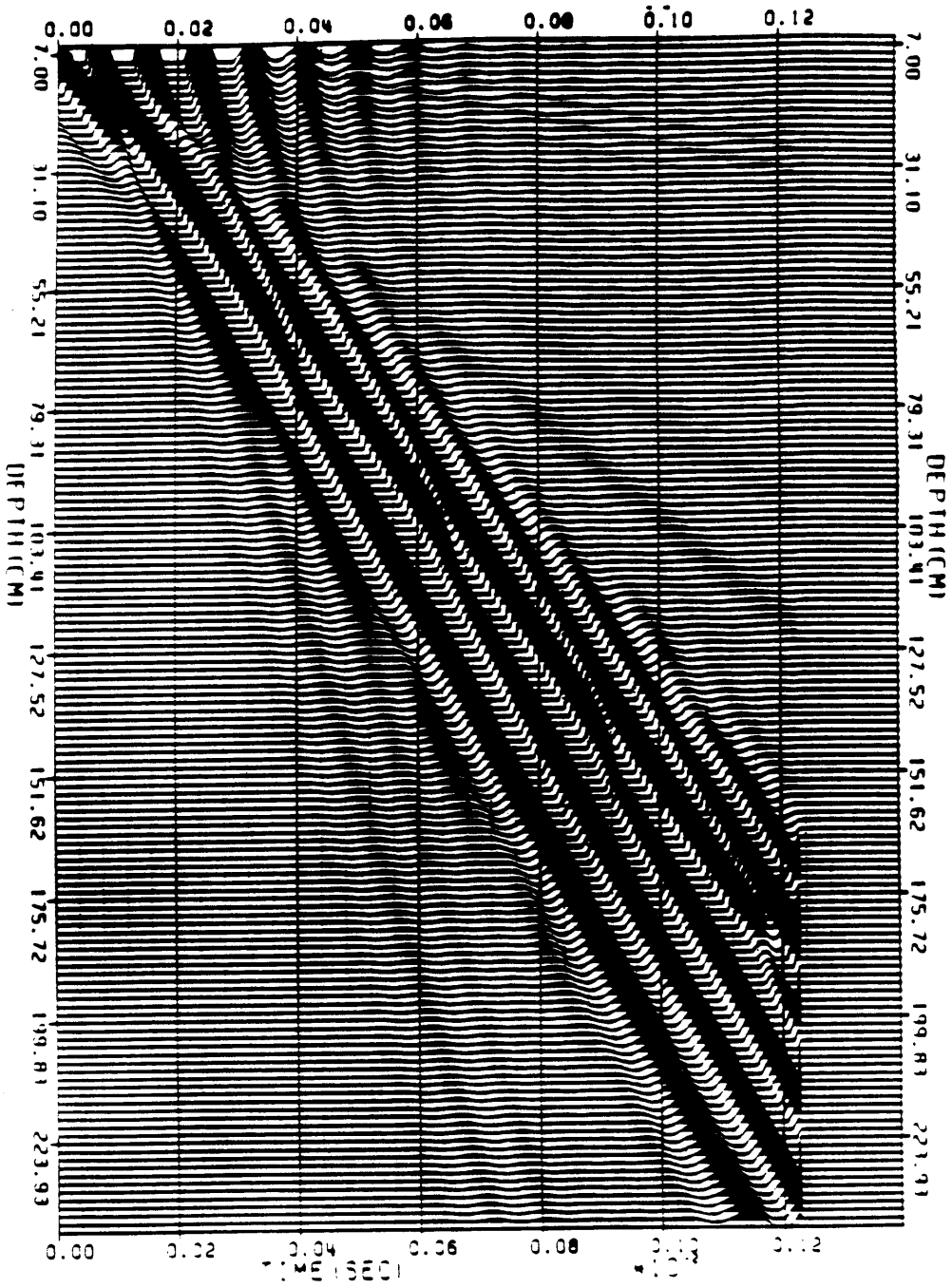
0.00
0.02
0.04
0.06
0.08
0.10
0.12
7.00
31.10
55.21
79.31
103.41
127.52
151.62
175.72
199.81
223.93
DEPTH(CM)
TIME(SEC)

Figure 20

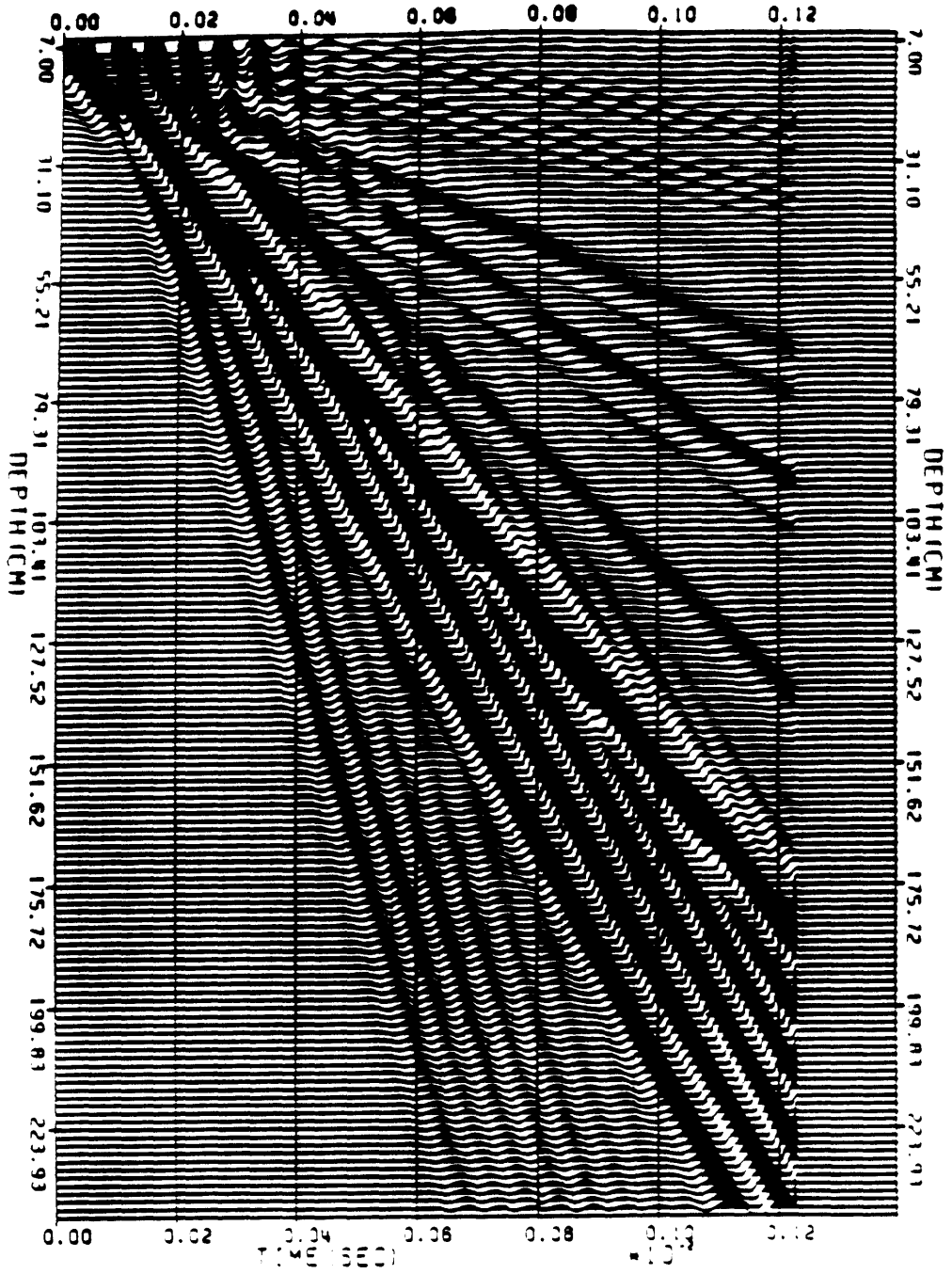
0.00
0.02
0.04
0.06
0.08
0.10
0.12
7.00
31.10
55.21
79.31
103.41
127.52
151.62
175.72
199.83
223.93
DEPTH(CM)

Figure 21

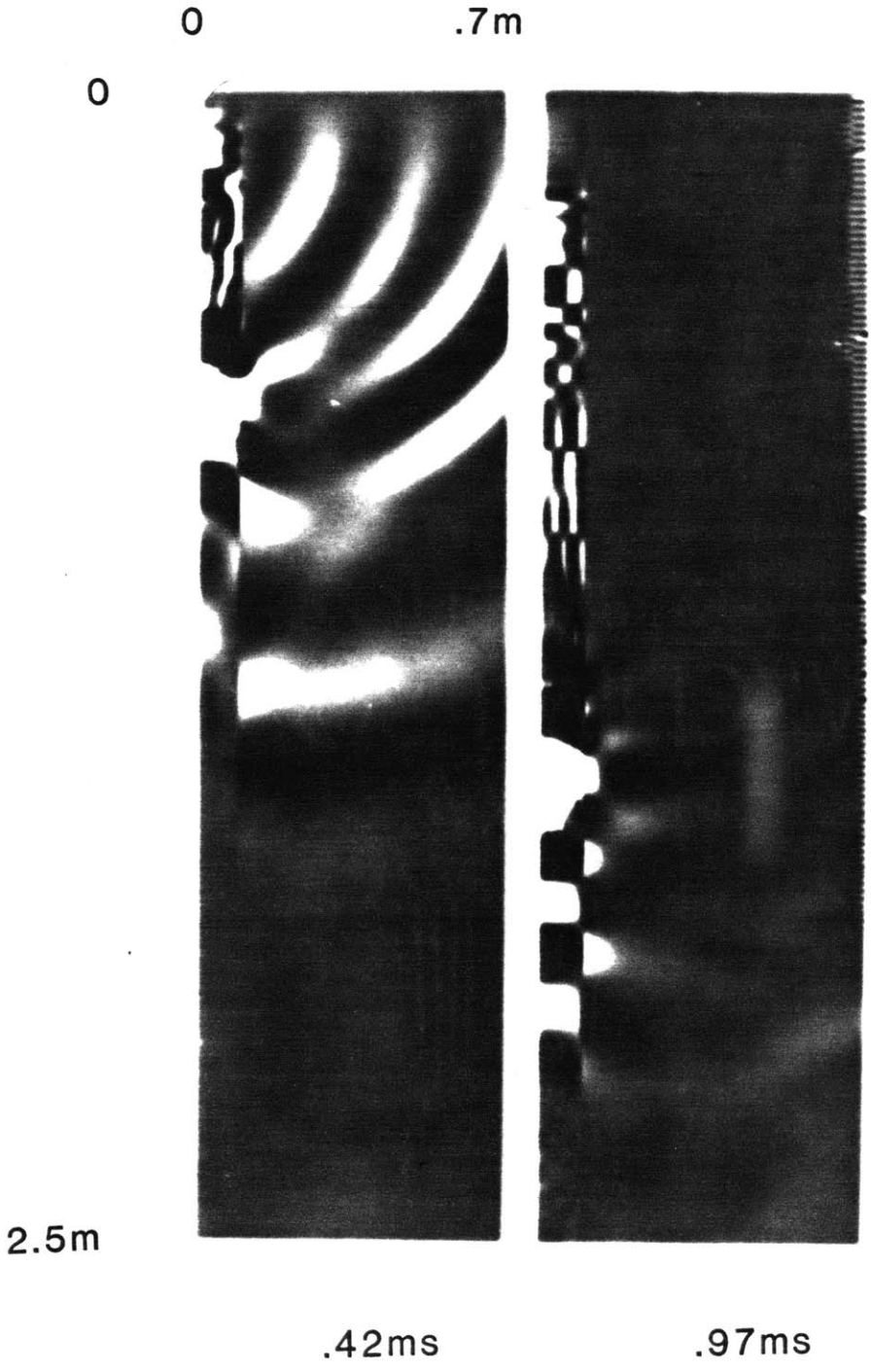

Figure 22

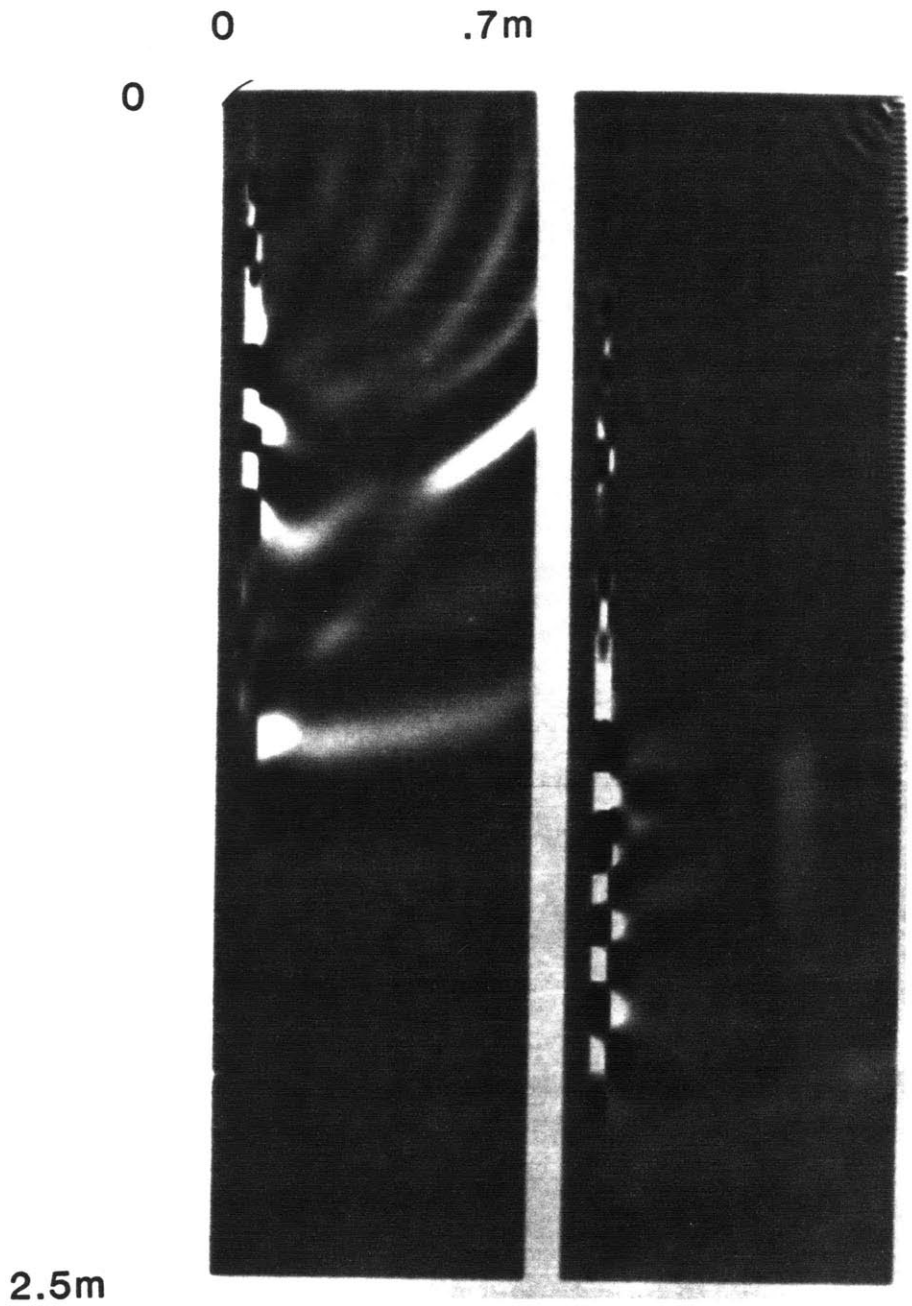

Figure 23

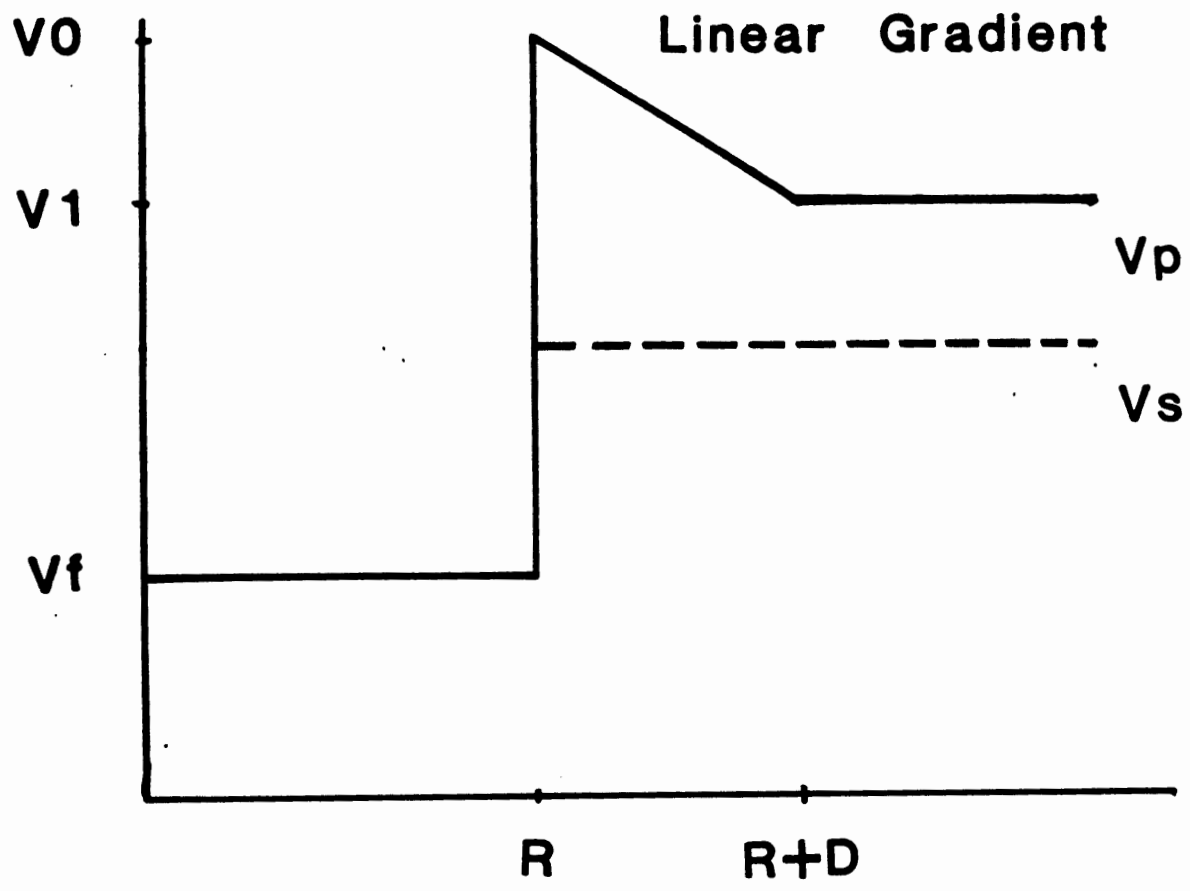

Figure 24

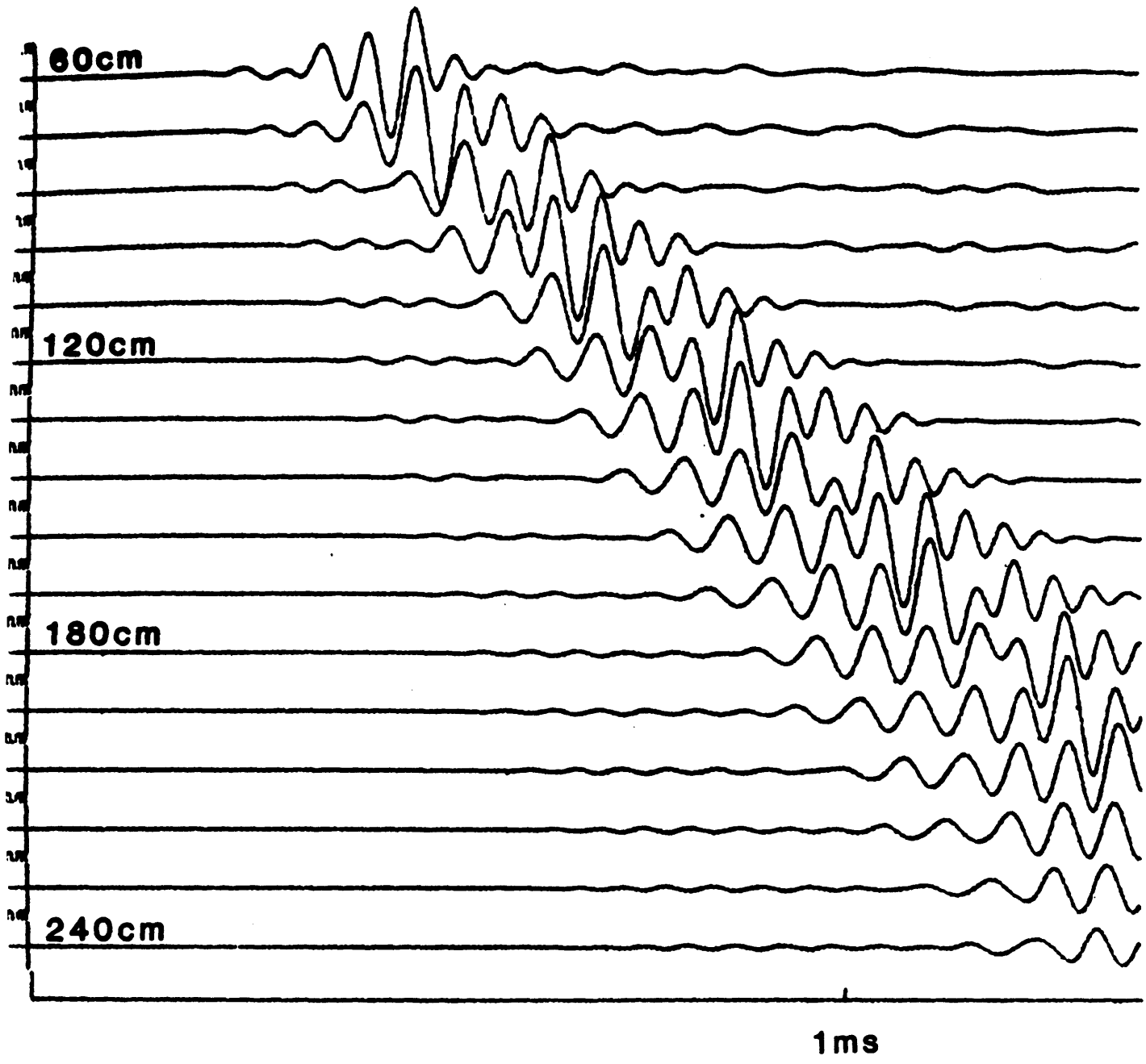

Figure 25

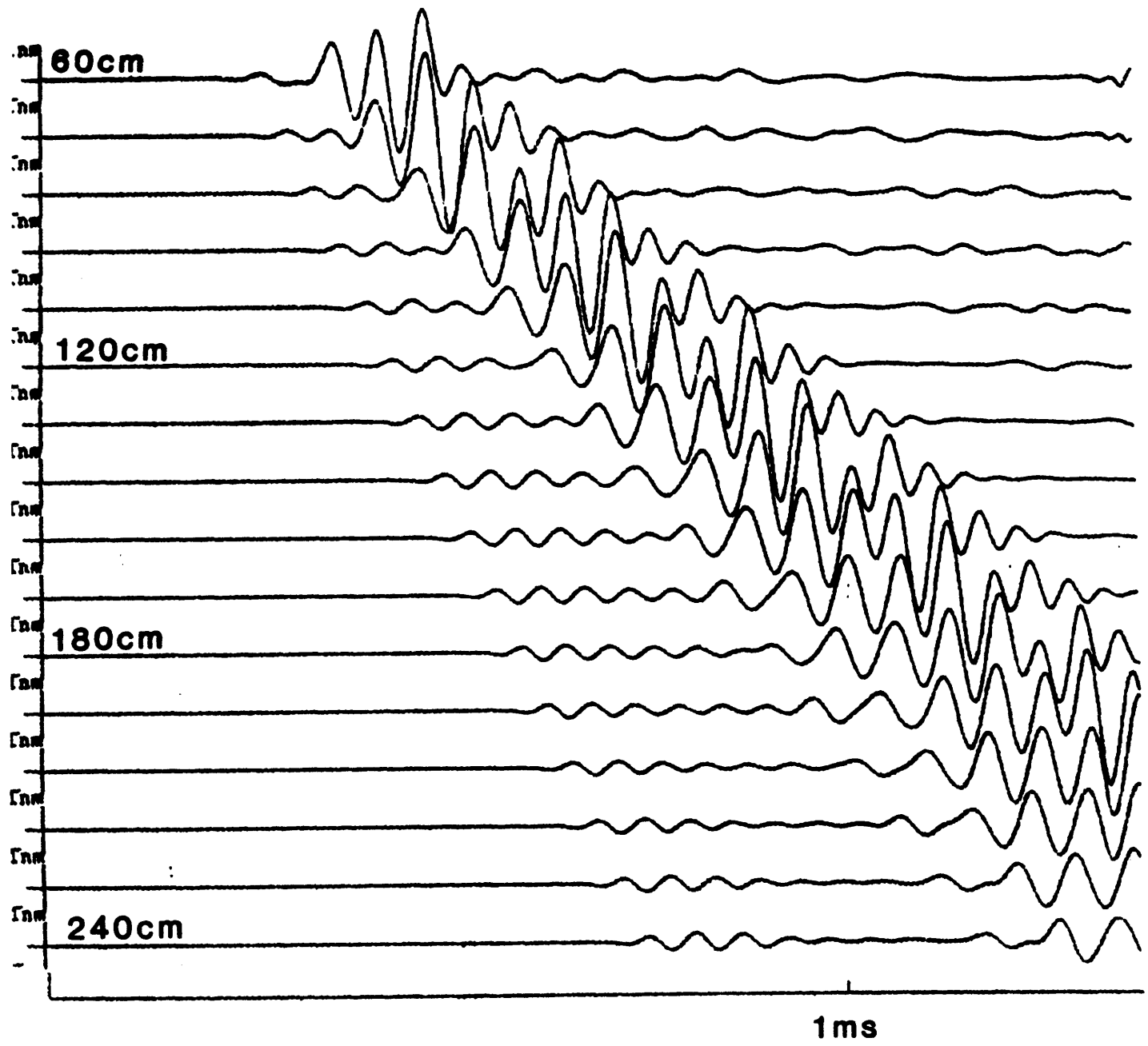

Figure 26

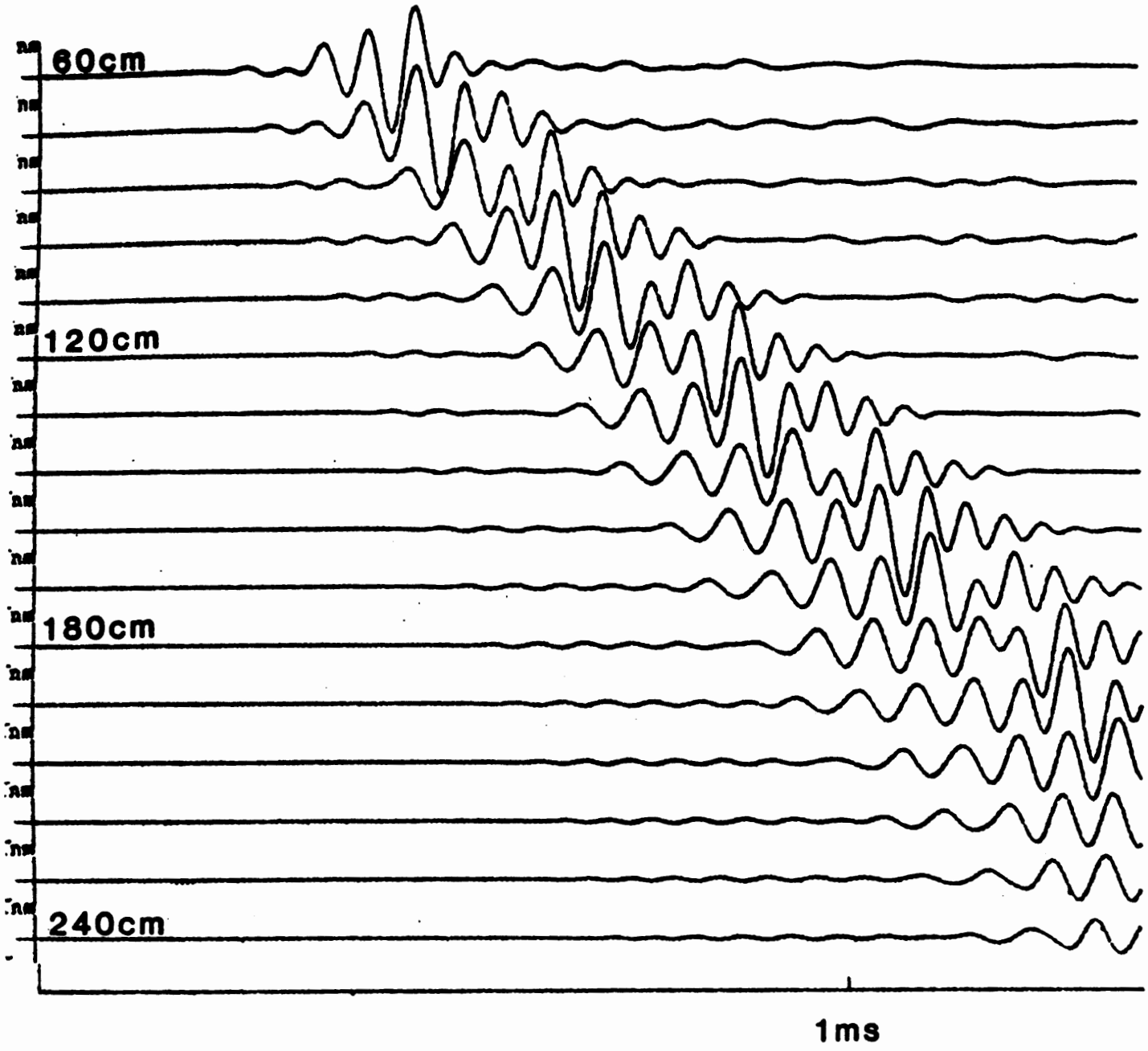

Figure 27

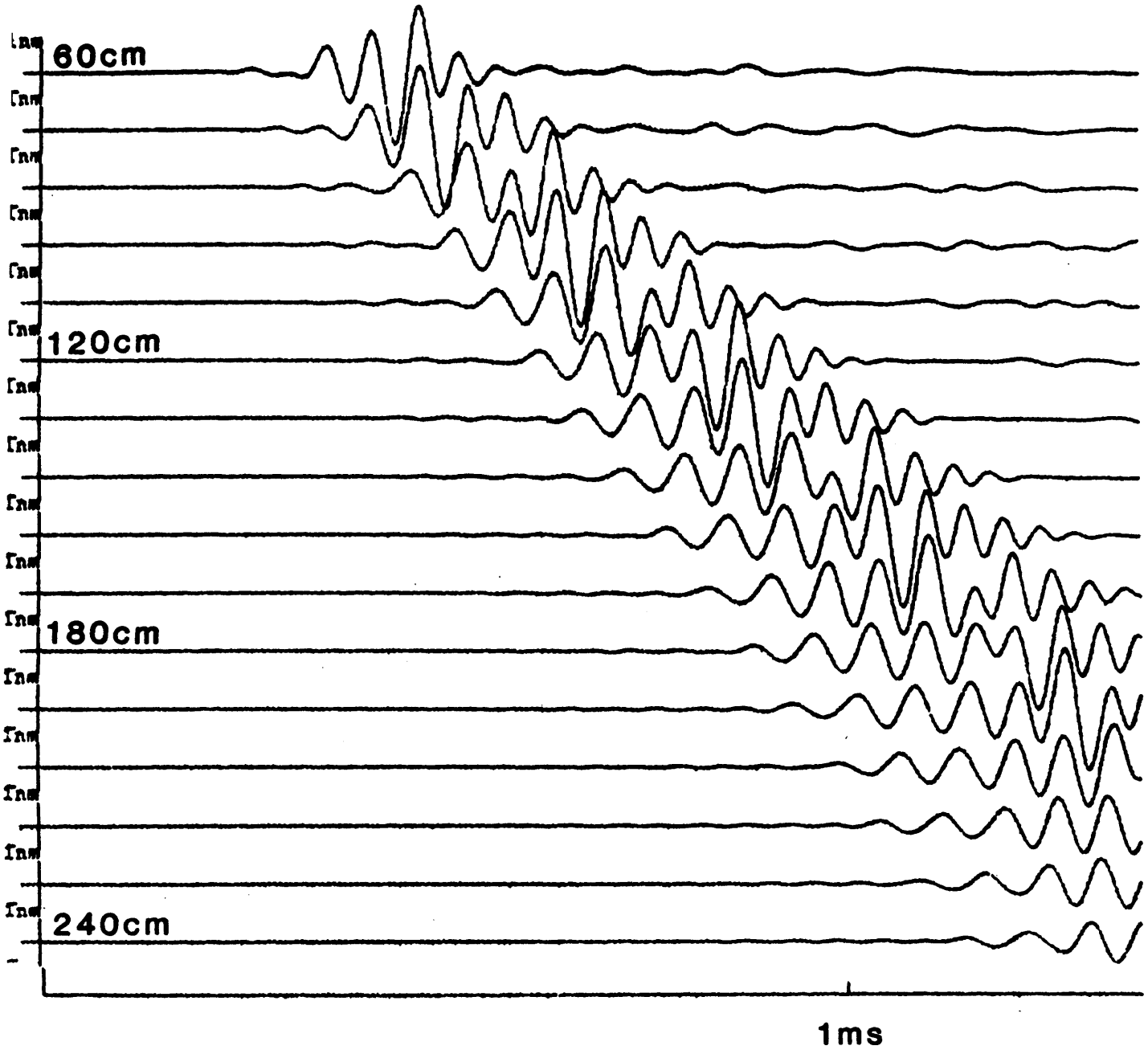

Figure 28

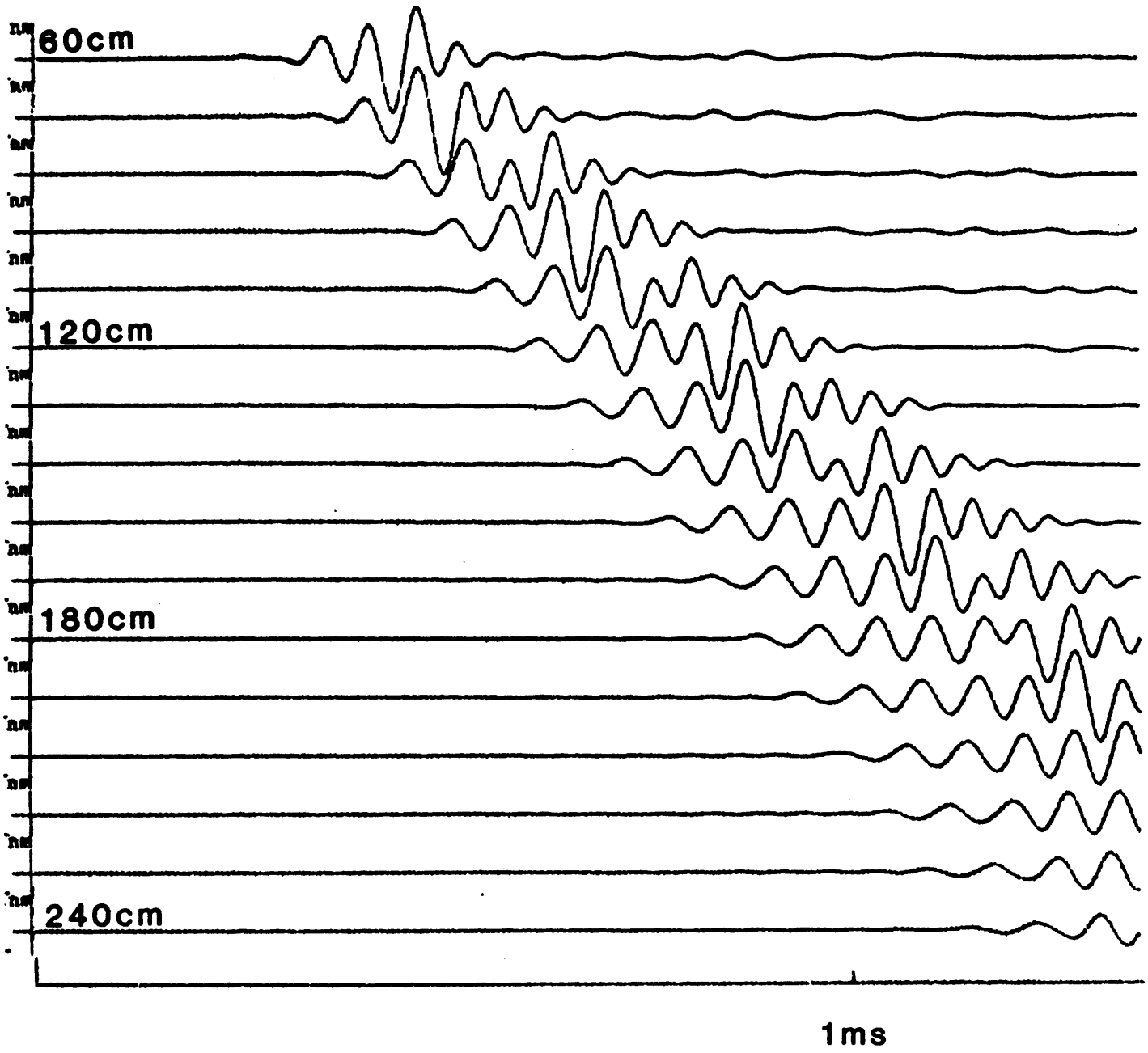

Figure 29

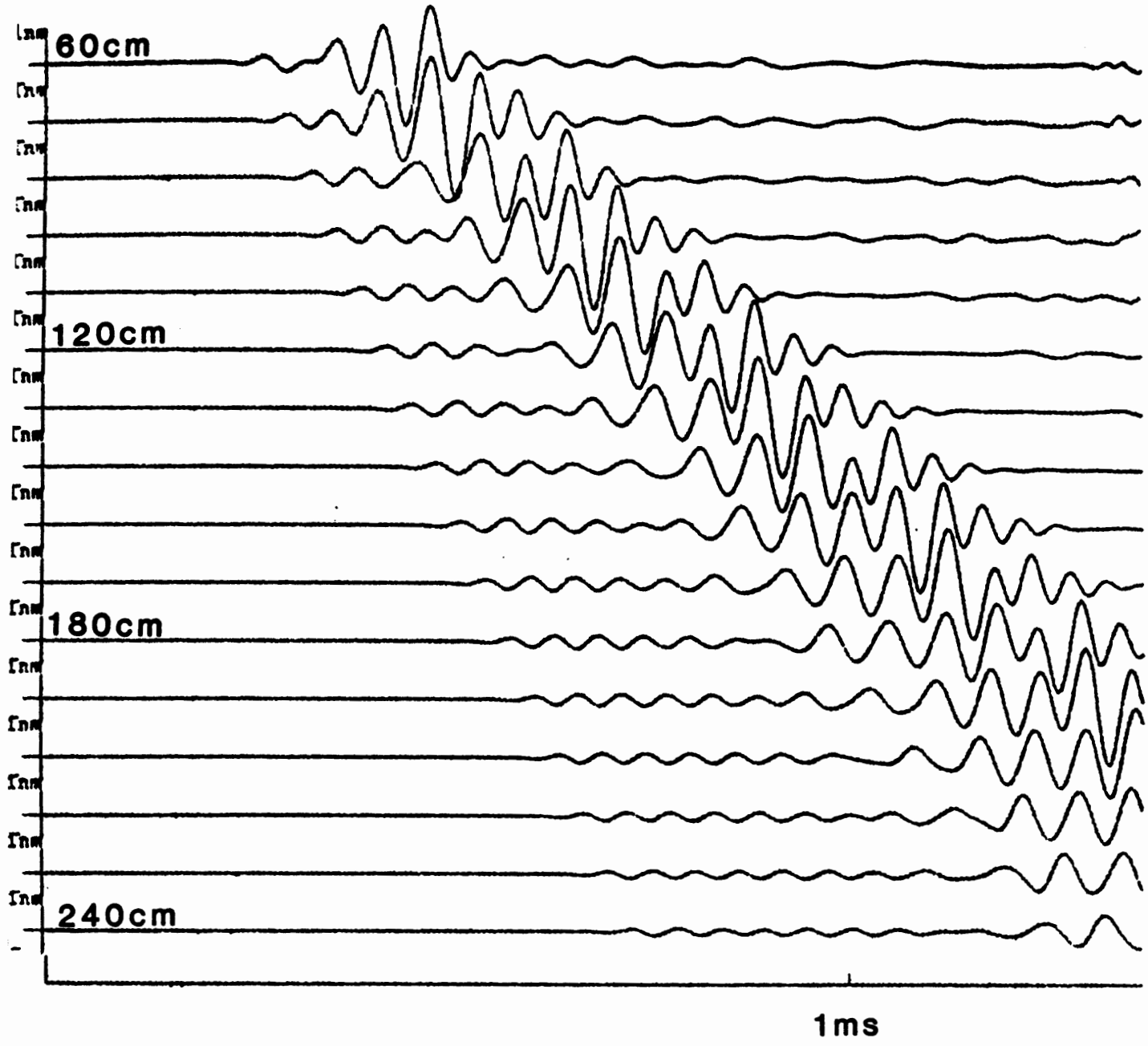

Figure 30

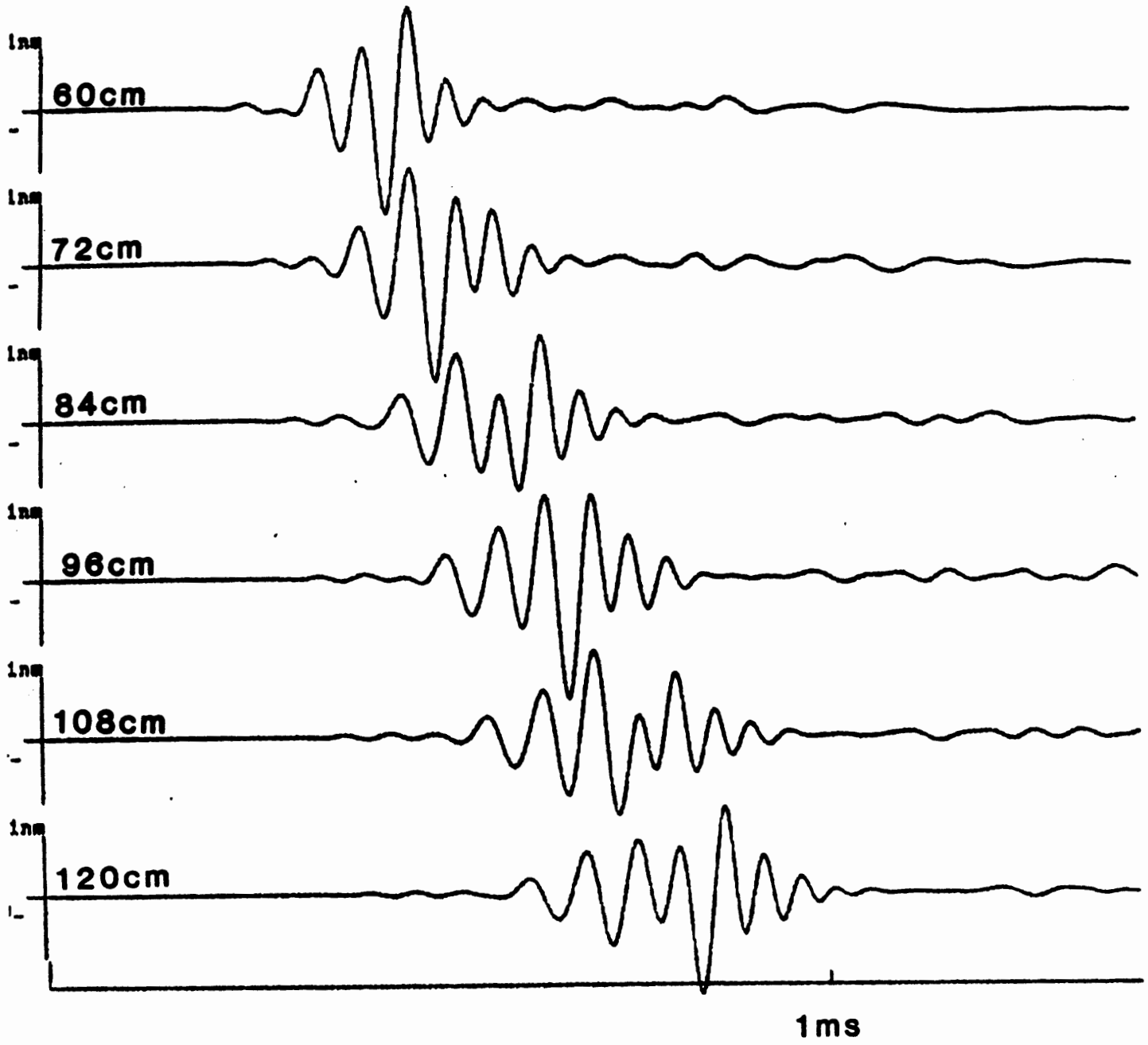

Figure 31